

EVAPORATION OF LOW-MASS PLANET ATMOSPHERES: MULTIDIMENSIONAL HYDRODYNAMICS WITH CONSISTENT THERMOCHEMISTRY

LILE WANG¹, FEI DAI^{1,2}
Draft version October 12, 2017

ABSTRACT

Direct and statistical observational evidences suggest that photoevaporation is important in eroding the atmosphere of sub-Neptune planets. We construct full hydrodynamic simulations, coupled with consistent thermochemistry and ray-tracing radiative transfer, to understand the physics of atmospheric photoevaporation caused by high energy photons from the host star. We identify a region on the parameter space where a hydrostatic atmosphere cannot be balanced by any plausible interplanetary pressure, so that the atmosphere is particularly susceptible to loss by Parker wind. This region may lead an absence of rich atmosphere (substantially H/He) for planets with low mass ($M \lesssim 3 M_{\oplus}$). Improving on previous works, our simulations include detailed microphysics and a self-consistent thermochemical network. Full numerical simulations of photoevaporative outflows shows a typical outflow speed $\sim 30 \text{ km s}^{-1}$ and $\dot{M} \sim 4 \times 10^{-10} M_{\oplus} \text{ yr}^{-1}$ for a $5 M_{\oplus}$ fiducial model rocky-core planet with 10^{-2} of its mass in the atmosphere. Supersonic outflows are not quenched by stellar wind ram pressure (up to 5 times the total pressure at transonic points of the fiducial model). The outflows modulated by stellar wind are collimated towards the night side of the planet, while the mass loss rate is only $\sim 25\%$ lower than the fiducial model. By exploring the parameter space, we find that EUV photoionization is most important in launching photoevaporative wind. Other energetic radiation, including X-ray, are of secondary importance. The leading cooling mechanism is ro-vibrational molecular cooling and adiabatic expansion rather than recombination or Ly α cooling. The wind speed is considerably higher than the escape velocity at the wind base in most cases, hence the mass loss rate is proportional to the second power of the EUV photosphere size R_{EUV} , instead of the third, as suggested by previous works. By calculating the evaporation timescale for a grid of planet models, we find a significant reduction in the atmosphere for planets with $M \lesssim 6 M_{\oplus}$. We then propose a semi-empirical scaling relation for mass loss rate as a function of high energy irradiation, planet mass and envelope mass fraction, with error mostly $\lesssim 20\%$. This allows us to reproduce the observed bimodal radius distribution of sub-Neptune Kepler planets semi-quantitatively.

Subject headings: planets and satellites: atmospheres — planets and satellites: composition — planets and satellites: formation — planets and satellites: physical evolution — astrochemistry — method: numerical

1. INTRODUCTION

Kepler has revealed a new class of planets with radii less than $4 R_{\oplus}$ and often with orbital distance closer than those of Mercury (e.g. Borucki et al. 2011; Marcy et al. 2014). These planets, colloquially known as the sub-Neptunes/super-Earths, were shown to be dominant outcome of planet formation despite that there is no analogue in our solar system. The ambiguity in the nomenclature highlights our ignorance about the composition of these planets. Are they terrestrial planets with a tenuous atmosphere or are they icy giants with a thick H/He envelopes? Over the past few years, radial velocity measurements and transit timing variation analysis have revealed the masses of ~ 80 of these sub-Neptunes. It has been suggested by Rogers (2015) that $1.6 R_{\oplus}$ represents a transition radius where planets smaller than this radius are predominantly rocky, whereas planets larger than this radius either contain significant volatiles such as water or are enclosed in a substantial H/He envelopes. Are planets formed with such a division in composition?

Or were they sculpted by various processes during the evolution? In this work, we investigate the influence of photoevaporation in shaping the observed properties of sub-Neptunes.

When the planet gravitational potential well is not too deep ($M \lesssim 60 M_{\oplus}$, e.g. Owen & Jackson 2012), incident irradiative photons are able to deposit sufficient energy into gas particles in the atmosphere, so that they can escape from the potential well, resulting in obvious photoevaporation (see also Lammer et al. 2003; Yelle 2004; Tian et al. 2005; Lecavelier Des Etangs 2007; Sanz-Forcada et al. 2011). Direct evidences of planet photoevaporation have been reported. These include “hot Jupiters” (e.g. Sanz-Forcada et al. 2011), and sub-Neptune planets (e.g. Ehrenreich et al. 2015). In addition, recent observation showing bimodal distribution of transiting planet radii (Fulton et al. 2017; Dong et al. 2017). This bimodality has been predicted by Owen & Wu (2013) and Lopez & Fortney (2014) as a consequence of photoevaporation, and further discussed by e.g. Owen & Wu (2017) (OW17 hereafter) and Jin & Mordasini (2017).

Models with hydrodynamics and microphysics have been constructed to understand the physics of evaporating planet atmosphere. Murray-Clay et al. (2009)

¹ Princeton University Observatory, Princeton, NJ 08544

² Department of Physics and Kavli Institute for Astrophysics and Space Research, Massachusetts Institute of Technology, Cambridge, MA 02139

(hereafter M-CCM09) constructed semi-analytic models of photoevaporation, assuming spherical symmetry, for “hot Jupiters”. This scenario is extended to more complicated dynamics by including X-ray in Owen & Jackson (2012). In this work, we will also construct a semi-analytic model to help us develop ideas about the basic physical picture of photoevaporation. Numerical models have also been constructed by previous works. Tripathi et al. (2015) simulated the evaporation of a model hot Jupiter in three dimensions, featuring the dynamics of photoevaporation outflow and interactions with orbital motion. Two-dimensional simulation in Christie et al. (2016) focused on the interaction with the ram pressure of stellar wind. Carroll-Nellenback et al. (2017) studied on the eventual fate of the outflow as an evaporating planet orbits around the central star. Due to the prohibitive computational costs to evolve a complete thermochemical network, those models consist only of a minimal set of reactions, i.e. photoionization/photodissociation of atomic hydrogen and Ly α cooling, or simply uses a one-to-one mapping of gas temperature to local ionization parameter by radiation.

The main focus of this work is the combination of consistent thermochemistry with hydrodynamics for modeling the photoevaporation of planets. We use a mid-scale chemical network (24 species, including neutral and singly charged dust grains) that was proved effective for modeling thermodynamic processes in protoplanetary disks (Wang & Goodman 2017, WG17 hereafter). We assume that the typical components in protoplanetary disks, as the birthplace of planets, should be similar to a primordial planetary atmosphere. Hydrodynamics in 2.5-dimensions (with axisymmetry) is coupled with time-dependent ray-tracing radiative transfer and thermochemistry in every cell across the simulation domain. Non-equilibrium processes are treated properly. Those costly calculations can be finished within a reasonable “wall-clock time” by utilizing the power of graphics processing units (GPUs hereafter). With these simulations, we expect to achieve better understanding of the microphysics and hydrodynamics relevant to photoevaporation, and probably yield predictions and/or explanations to observables.

This paper is structured as follows. §2 presents the static atmosphere model without any irradiation as the initial conditions of our numerical simulations, and discusses the implications of those hydrostatic models. §3 construct spherical symmetric semi-analytic models with minimal thermochemistry, showing the caveats of them which necessitates proper numerical simulations. In §4 we describe the methods of our numerical simulations. §5 presents the setup and results of the fiducial model. In §6 we explore and elaborate the effects of different physical parameters. §7 discusses the implications and applications of our photoevaporation models. §8 concludes and summarizes the paper. Details of mathematical derivations are provided in the appendices.

2. HYDROSTATICS OF PLANET ATMOSPHERE

The hydrostatic structures of planet atmospheres are discussed in this section, as the initial condition and inner boundary conditions of our further numerical explorations on photoevaporation. In what follows, we will use the terms “atmosphere” and “envelope” interchangeably.

We start with a solid core as the inner supporter and the source of gravity of the atmosphere. The mass-radius relation approximately obeys $M_c \propto R_c^4$ (see also Lopez & Fortney 2014). We adopt the terrestrial mean density at $1 M_\oplus$, $\rho(M_c = M_\oplus) = 5.5 \text{ g cm}^{-3}$, unless specially noted. Outside the solid core lies the atmosphere. The atmosphere of a planet has two segments: an adiabatic, convective interior and an (approximately) isothermal, radiative exterior (e.g. Rafikov 2006; Owen & Wu 2016; Ginzburg et al. 2016). Due to incident radiation from the central star at bolometric luminosity L_* , the temperature of the roughly isothermal exterior for a planet at semi-major axis a satisfies,

$$T \simeq T_{\text{eq}} = 886 \text{ K} \left(\frac{L_*}{L_\odot} \right)^{1/4} \left(\frac{a}{0.1 \text{ AU}} \right)^{-1/2}. \quad (1)$$

Transition from adiabatic to isothermal occurs when eq. (1) is equated to the temperature in eq. (2), marked by subscript “rcb” (short for “radiative-convective boundary”) attached to pertinent physical quantities.

2.1. Convective (adiabatic) interior

The adiabatic equation of state (EoS) of gas reads $p = K\rho^\gamma$, where p is the gas pressure, ρ the mass density, γ the adiabatic index, and K a constant related to the specific entropy. We neglect the self gravity of the envelope. The temperature and density profiles in the adiabatic layer are given by,

$$T = T_0 \left[1 + \beta_{\text{ad}} \left(\frac{R_c}{r} - 1 \right) \right]; \quad \rho = \rho_0 \left(\frac{T}{T_0} \right)^{1/(\gamma-1)}; \\ \beta_{\text{ad}} \equiv \nabla_{\text{ad}} \left(\frac{GM_c \mu}{R_c k_B T_0} \right); \quad \nabla_{\text{ad}} \equiv \left(\frac{\gamma-1}{\gamma} \right). \quad (2)$$

Here μ is the (dimensional) mean molecular mass, G the gravitational constant, M_c and R_c the mass and radius of the solid core beneath the atmosphere respectively, T_0 and ρ_0 temperature and density at the bottom of adiabatic atmosphere ($r = R_c$) respectively. ∇_{ad} is the adiabatic gradient, and β_{ad} measures gravitational binding energy against gas energy: the adiabatic inner envelope is gravitationally unbounded if $\beta_{\text{ad}} \leq 1$, which is not discussed in this paper.

As the total mass of isothermal layer is ill-defined (and practically small compared to the mass in the adiabatic layer; see §2.2), we characterize the envelope mass by the mass of the adiabatic segment, by integrating from $r = R_0$ to r_{rcb} ,

$$M_{\text{ad}} = 4\pi \int_{R_c}^{r_{\text{rcb}}} \rho r^2 dr \\ = 4\pi R_c^3 \rho_{\text{rcb}} \left[\nabla_{\text{ad}} \left(\frac{GM_c \mu}{R_c k_B T_{\text{eq}}} \right) \right]^{\frac{1}{\gamma-1}} \left(\frac{\beta_{\text{ad}}}{\beta_{\text{ad}} - 1} \right)^{\frac{3\gamma-4}{\gamma-1}} \\ \times \mathcal{B} \left[\left(\frac{\beta_{\text{ad}} - 1}{\beta_{\text{ad}}} \right) x; \frac{3\gamma-4}{\gamma-1}, \frac{\gamma}{\gamma-1} \right]_{x=1}^{x=r_{\text{rcb}}/R_c}, \quad (3)$$

where

$$\mathcal{B}(x; a, b) \equiv \int_0^x dt t^{a-1} (1-t)^{b-1}, \quad (4)$$

is the incomplete beta function.

2.2. Radiative (isothermal) exterior and model calibration

The isothermal layer the density profile is given by,

$$\rho = \rho_{\text{rcb}} \exp \left[\beta_{\text{iso}} \left(\frac{r_{\text{rcb}}}{r} - 1 \right) \right] \geq \rho_{\text{rcb}} e^{-\beta_{\text{iso}}} ; \quad (5)$$

$$\beta_{\text{iso}} = \frac{GM_c \mu}{r_{\text{rcb}} k_B T_{\text{eq}}} .$$

ρ converges to a finite constant at $r \rightarrow \infty$; the integration of gas mass diverges at infinite radius. We setup the initial atmosphere of a planet by comparing gas pressure at infinite radius in the isothermal layer to the ambient pressure of e.g. stellar wind, nominally (\tilde{p} is the reference parameter characterizing the magnitude of ambient pressure),

$$p_{\text{amb}} \simeq \tilde{p} \times 10^{-8} \text{ dyn cm}^{-2} \left(\frac{a}{0.1 \text{ AU}} \right)^{-2} . \quad (6)$$

If $p_{\infty} \equiv (k_B T_{\text{eq}} \rho_{\text{rcb}} e^{-\beta_{\text{iso}}} / \mu) < p_{\text{amb}}$, the pressure in the isothermal segment is matched to the ambient pressure at a finite radius. In this case, the mass of the isothermal region, estimated from $r = r_{\text{rcb}}$ to where $p = p_{\text{amb}}$, is generally $\lesssim 10^{-1}$ of M_{ad} , and characterizing the mass of atmosphere with M_{ad} is well-defined. If $p_{\infty} > p_{\text{amb}}$, the isothermal envelope evaporates at a very short timescale by hydrodynamic mechanisms that are irrelevant to photoevaporation (see e.g. Owen & Wu 2016). The latter will be discussed in §2.3, and the former case is the focus of §4,

The radiative nature of the isothermal layer helps us to calibrate the model parameters. Given M_c and R_c , a pair of (ρ_0, T_0) uniquely determines the hydrostatics of atmosphere, but those quantities are difficult to map directly onto the physics. In order to express those crucial parameters more explicitly, here we follow the scheme in OW17 with some simplifications. At the radiative-convective boundary, the adiabatic gradient of $\ln T$ is related to the luminosity of cooling by continuum of the planet L ,

$$\left. \frac{d \ln T}{dr} \right|_{r_{\text{rcb}}} = - \frac{GM_c \mu}{k_B T_{\text{eq}} r_{\text{rcb}}^2} = - \left(\frac{L}{4\pi r_{\text{rcb}}^2} \right) \left(\frac{3\kappa \rho_{\text{rcb}}}{16\sigma T_{\text{eq}}^4} \right) , \quad (7)$$

where σ here is the Stefan-Boltzmann constant, and κ is the Rosseland mean opacity. We adopt the fitting formula of κ , as a function of ρ and T (obtained by Rogers & Seager 2010, based on Freedman et al. 2008),

$$\kappa \simeq \kappa_0 \times \tilde{\kappa} \left(\frac{p}{\text{dyn cm}^{-2}} \right)^{\alpha} \left(\frac{T}{\text{K}} \right)^{\beta} ; \quad (8)$$

$$\kappa_0 \equiv 10^{-7} \text{ cm}^2 \text{ g}^{-1} , \quad \alpha \equiv 0.45 , \quad \beta \equiv 0.68 .$$

Our ignorance about L , as well as the uncertainty in the dimensionless opacity parameter $\tilde{\kappa}$, are absorbed into a parameter with the dimension of time,

$$\tau_{\text{KH}} \equiv \frac{GM_c M_{\text{ad}}}{R_c L \tilde{\kappa}} . \quad (9)$$

This τ_{KH} is indeed the Kelvin-Helmholtz timescale of planet atmosphere with $\tilde{\kappa}$ absorbed. From eq. (7) we

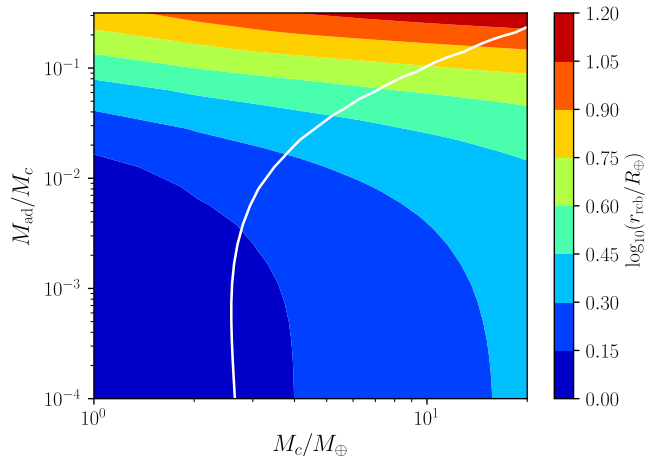


FIG. 1.— Radius of the radiative-convective boundary r_{rcb} , which roughly resembles the *observed* radius of planets, presented as a function of solid core mass M_c and envelope mass fraction characterized by M_{ad}/M_c (M_{ad} is the mass of the adiabatic atmosphere). The white curve overlaid indicates the limit at which the ambient pressure can marginally confine a hydrostatic atmosphere. The region on its upper left consists of models that would rapidly disperse their envelopes due to Parker wind. Note the critical core mass that occurs at $M_c \sim 3 M_{\oplus}$, which depends logarithmically on the luminosity of the host star, the core composition, and the ambient pressure.

have,

$$M_{\text{ad}} = \frac{64\pi\mu\sigma T_{\text{eq}}^3 R_c \tau_{\text{KH}}}{3k_B (p_{\text{rcb}}/\text{dyn cm}^{-2})^{\alpha} \kappa_0 (T_{\text{eq}}/\text{K})^{\beta} \rho_{\text{rcb}}} ;$$

$$\left(\frac{\rho_{\text{rcb}}}{10^{-3} \text{ g cm}^{-3}} \right)^{\alpha+1}$$

$$= [10^{-1-3\beta} (3.51 \times 10^7)^{1-\alpha}] \times \left(\frac{M_{\text{ad}}}{0.104 M_{\oplus}} \right)^{-1}$$

$$\times \left(\frac{R_c}{R_{\oplus}} \right) \left(\frac{\tau_{\text{KH}}}{10^8 \text{ yr}} \right) \left(\frac{\mu}{2.35 m_p} \right)^{\alpha+1} \left(\frac{T_{\text{eq}}}{10^3 \text{ K}} \right)^{3-\alpha-\beta} . \quad (10)$$

For fixed M_c and R_c , we first take M_{ad} and τ_{KH} as input parameters, then use eq. (10) to find out ρ_{rcb} , before inserting those quantities into eq. (3) to solve for β_{ad} numerically, utilizing eq. (2). Those steps allows us to determine atmospheric profiles of the planet as a function of envelope mass fraction and the Kelvin-Helmholtz timescale.

2.3. Mass loss with unbalanced ambient pressure

We present examples of hydrostatic models in Figure 1. Model parameters are: $\tau_{\text{KH}} = 10^8 \text{ yr}$, $T_{\text{eq}} = 886 \text{ K}$, $\mu = 2.35 m_p$ (m_p is the mass of proton), and $\tilde{p} = 1$. Note the overlaid white curve indicating the critical conditions of pressure balancing, above which the models have $p_{\infty} > p_{\text{amb}}$ and thus the atmosphere is expected to lose mass rapidly. The approximate mass loss rate by Parker wind mechanism, assuming sufficient energy supply to maintain an isothermal outflow, is estimated by (subscript “s” denotes the sonic surface; for estimating

ρ_s see e.g. Parker 1958),

$$\dot{M}_{\text{Parker}} = 4\pi R_s^2 \rho_s c_s ; \quad R_s = \frac{GM_c}{2c_s^2} ; \quad (11)$$

$$\rho_s \sim \rho_{\text{rcb}} \exp \left[-\frac{R_s}{r_{\text{rcb}}} \left(1 - \frac{r_{\text{rcb}}}{R_s} \right)^2 \right] .$$

On the other hand, the rate of energy injection by the bolometric luminosity L_* of the host star (not to be confused with photoevaporation by high energy photons, L_{HE}) is also limiting hydrodynamic mass loss rate. The energy-limited mass loss rate \dot{M}_{ene} is approximately (note that πr_{rcb}^2 is roughly the area of intercepting stellar radiation in optical and infrared, and a is the semi-major axis of the planet orbit),

$$\dot{M}_{\text{ene}} \sim \left(\frac{L_*}{4\pi a^2} \right) \pi r_{\text{rcb}}^2 \left(\frac{c_s^2}{2} \right)^{-1} ; \quad (12)$$

$$\dot{M} \sim \min\{\dot{M}_{\text{Parker}}, \dot{M}_{\text{ene}}\} .$$

The evaporation timescale of the adiabatic atmosphere is approximately $t_{\text{evap}} \equiv M_{\text{ad}}/\dot{M} \gtrsim 10^2$ yr for planets with $M_{\text{ad}}/M_c \gtrsim 10^{-2}$. Envelope of a planet evaporates until it reaches the curve if M_c is greater than the critical value $M_{\text{crit}} \sim 2.5 M_{\oplus}$, or otherwise totally loses its adiabatic segment of envelope. For rocky-core planets, we varied \tilde{p} by ± 4 orders of magnitude to confirm that the value of M_{crit} varies within the range of $2 \lesssim (M_{\text{crit}}/M_{\oplus}) \lesssim 3$, which depends on the logarithm (thus very insensitively) of \tilde{p} and T_{eq} , as one can infer from eq. 6. We refer the reader to §7.3 for examples of evaporation timescale in this region.

This critical mass quantitatively agrees with the observed absence of massive H/He planetary atmosphere for less massive planets with $M \lesssim 3 M_{\oplus}$ (e.g. Rogers 2015; Zeng et al. 2016; López-Morales et al. 2016). We hence suggest that the inability of low mass planets to have its atmosphere pressure balanced by the ambient would be possible to result in those observation constraints. Similar mechanisms are also suggested in Owen & Wu (2016) to shape a similar limit.

This would suggest that planets with $M_c \lesssim 3 M_{\oplus}$ would lose its primordial H/He atmosphere quickly after the disk disperses (after 10^{6-7} yr). In other words, planets in this mass range will not have a substantial H/He envelope ($< 10^{-4}$ by mass) unless subsequent outgassing is significant. Owen & Wu (2016) reached a similar conclusion but did not offer an quantitative prediction on the threshold. We will show in §7, that observational test of this prediction is more complicated. This is because planets with core masses between $\sim 3 M_{\oplus}$ to $\sim 6 M_{\oplus}$ (the upper boundary is more sensitive to the specific choices of parameters) may be stable to Parker Wind outflow but still susceptible to photoevaporation. On a $\sim 10^8$ yr timescale, these planets will also lose their primordial H/He envelope photoevaporatively. Observationally, the $6 M_{\oplus}$ (or $\sim 1.6 R_{\oplus}$) threshold was pointed out by Dressing et al. (2015) and Rogers (2015).

3. FIRST IMPRESSION ON PHOTOEVAPORATION: SEMI-ANALYTIC MODELS

In this section we describe an analytic model with minimum (but adequate) hydrodynamics, radiative transfer

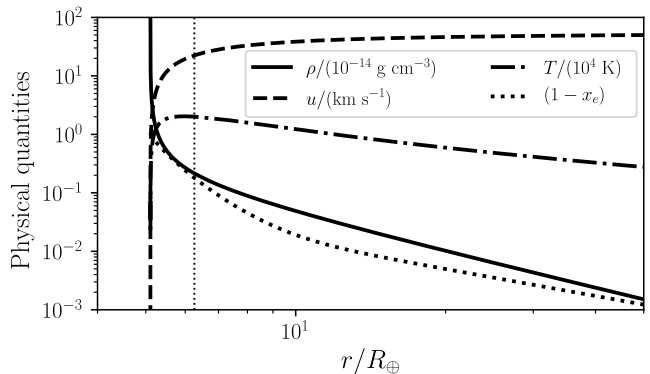
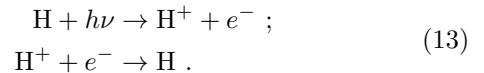


FIG. 2.— The radial profile of various quantities in the spherically symmetric analytical solution of a $5 M_{\oplus}$, 10^{-2} envelope mass fraction at 0.1 AU, presented in §3.1. Mass density ρ , radial velocity u , temperature T , and neutral fraction $(1 - x_e)$ profiles are presented in different line styles, which are indicated in the legend. The vertical thin dotted line indicates the location where the flow is transonic.

and thermochemistry, to help us understand the process of photoevaporation. The procedures are similar to (but still subtly different from) M-CCM09, which are stated below and in Appendix A.

3.1. Guiding physics and example solution

We consider a spherically symmetric model with external gravity set by the co-centered solid core. The hypothetical configuration of stellar radiation is characterized by radiation flux $\vec{F} = -\hat{r}F_0$ in absence of absorption. This configuration of radiation field represents the radial column at the substellar point, and is also expected to characterize other radial columns semi-quantitatively. For simplicity we assume that radiation is monochromatic, and only take the following reactions into account,



At $h\nu = 25$ eV, the photoionization cross section is $\sigma \simeq 1.2 \times 10^{-18}$ cm² (Verner et al. 1996). We adopt the UMIST version of type-B recombination rate (McElroy et al. 2013), $\alpha_B \equiv \alpha_0(T/T_0)^\kappa$, where T_0 is some fiducial temperature, $\kappa \equiv -0.75$, and

$$\alpha_0 = 3.5 \times 10^{-12} \text{ cm}^3 \text{ s}^{-1} \left(\frac{T_0}{300 \text{ K}} \right)^\kappa . \quad (14)$$

Basic heating and cooling processes corresponding to the two reactions in eq. (13) are also introduced, including photoelectric heating with energy per reaction $\langle E_{\text{pe}} \rangle = h\nu - I_e$ ($I_e = 13.6$ eV is the ionization threshold of atomic hydrogen) for each hydrogen atom ionized, and recombination cooling energy loss $\langle E_{\text{rr}} \rangle = 3k_B T/2$ for each hydrogen atom reformed (k_B is the Boltzmann constant). Draine (2011) suggests that $\langle E_{\text{rr}} \rangle$ is smaller than $3k_B T/2$, since the electrons with lower kinetic energy are easier to be captured by ions. However, we still assume $\langle E_{\text{rr}} \rangle = 3k_B T/2$ for simplicity.

In Figure 2, we present an example of semi-analytic solutions. Following the construction procedures in Appendix A, this solution is matched (a) inwards to a $T_{\text{eq}} = 886$ K isothermal layer outside an $M_{\text{ad}} = 10^{-2} M_c$ adiabatic envelope at $r_{\text{min}} = 5.11 R_{\oplus}$ (where $\rho = 0.98 \times 10^{-13}$ g cm⁻³), surrounding an $M_c = 5 M_{\oplus}$, $R_c = 1.5 R_{\oplus}$

core (assuming envelope cooling timescale 10^8 yr), and (b) outwards to an $F_0 = 10^{15} \text{ cm}^{-2} \text{ s}^{-1}$ outer boundary (this is the radiation flux at $a = 0.1$ AU with EUV luminosity $10^{-3.5} L_\odot$ at $h\nu = 25$ eV). Considering the effective solid angle of intercepting EUV irradiation being π , the mass loss rate is estimated by $\dot{M} \sim (\pi r^2 \rho v)_{r_{\max}} \simeq 1.3 \times 10^{-9} M_\oplus \text{ yr}^{-1}$, thus $t_{\text{evap}} \sim 40$ Myr.

3.2. Steady versus static: Caveats and necessity of a consistent model

Straightforward as it may seem, the semi-analytic solution presented in the previous section still has caveats. To be mathematically rigorous, a steady state outflow solution has no hope to be *fully* matched to a static interior: the radial mass flux, being a finite constant in the steady outflow, must vanish in the static region. Typically this mismatch is interpreted by assuming that the static region quickly relaxes to new configurations as the gas at the wind base (definition see Appendix A) is removed by the outflow. The new configurations are almost identical to the original one as long as the evolution time $t \ll t_{\text{evap}}$, so that the location and hydrodynamic conditions of the wind base can be treated as invariant.

However, the equilibrium conditions beneath the wind base are impossible, with only hydrogen ionization and recombination processes included. Since $\langle E_{\text{pe}} \rangle \sim (k_B \times 10^5 \text{ K})$ is much greater than $\langle E_{\text{tr}} \rangle \lesssim (k_B \times 10^3 \text{ K})$, in case of $S_I = 0$ (ionization equilibrium), the local energy balance S_E is always appreciably positive (see also eqs. A2, A4). Ly α cooling, suggested by M-CCM09, is indeed negligible at the temperature and density beneath the wind base for our low-mass planet models. As a result, the timescale at which a fluid element in the static region doubles its temperature is estimated by $t_{\text{heat,static}} \sim 10 \text{ s} \times [F/(10^{15} \text{ cm}^{-2} \text{ s}^{-1})]^{-1}$, which is merely one day even if the EUV flux F is suppressed by 4 orders of magnitude compared to the unattenuated flux F_0 . As soon as a fluid element is heated, it expands and allows more EUV radiation to come in, which in turn speeds up the heating process before this fluid element finally migrates into the wind. As a result, the eroded static layer never recovers its original configuration; instead, the location of wind base moves inwards in a relatively short period of time compared to t_{evap} . The wind base shrinks until it reaches a very high density so that the speed of erosion is comparable to t_{evap} . In fact, using the code described in §4 in spherically symmetric configuration and identical thermochemistry as in §(3.1), we figure out that the wind base moves from $\rho \sim 10^{-13} \text{ g cm}^{-3}$ to $\rho \sim 10^{-6} \text{ g cm}^{-3}$ within $t \lesssim 0.1$ yr, while the mass loss rate roughly halves as the effective area of intercepting EUV radiation shrinks (the mass of isothermal layer in the range of $10^{-13} \text{ g cm}^{-3} < \rho < 10^{-6} \text{ g cm}^{-3}$ is only $\sim 10^{-10} M_\oplus$). At each instant the wind region can still be perfectly fit by a semi-analytic solution (mathematically thanks to the extra degree of freedom, see the discussions in Appendix A; note that the timescales for a wind configuration to relax is $r_{\max}/v_{\text{wind}} \sim 10^4 \text{ s}$, which is still tiny compared to the erosion timescale).

In summary, the assumption of quasi-invariant static region matching a steady state wind with hydrogen only leads to contradictions. Therefore we need numerical models where detailed microphysics are coupled consis-

tently with full hydrodynamics, preferably in multiple dimensions.

4. NUMERICAL SIMULATION METHODS

We present the numerical methods for modeling photoevaporation of planet atmosphere in this section. Those schemes are close to WG17 as underlying physical processes are similar (see §1).

4.1. Fluid mechanics

Full hydrodynamics is included using the general-purpose grid-based astrophysical simulation code *Athena++* (White et al. 2016; J. Stone et al., in preparation). Despite its capability of solving MHD problems, we neglect magnetic fields for now, using the HLLC Riemann solver, van Leer reconstruction with revised slope limiter for improved order of accuracy (see Mignone 2014), and Consistent Multi-fluid Advection (CMA) for strict conservation of chemicals inside advecting fluids (e.g. Glover et al. 2010).

4.2. Radiative transfer

High energy photons from the host star is the key to photoevaporation. We use four representative energy to portray the influence of those photons: $h\nu = 7$ eV for FUV photons (“soft FUV”) that do not interact with hydrogen or helium, $h\nu = 12$ eV for the Lyman-Werner (LW) photons, $h\nu = 25$ eV for the EUV photons, and $h\nu = 1$ keV for the X-ray. For high energy photons in those energy bins, absorption processes overwhelm scattering (Verner & Yakovlev 1995; Verner et al. 1996; Draine 2011), with two potential exceptions: hard X-ray and Ly α . Scattered hard X-ray photons could affect ionization and thus magnetic coupling in regions beyond the reach of photons in other energy bands (e.g. Igea & Glassgold 1999; Bai & Goodman 2009). We ignore their effects for two reasons: (a) that magnetic fields are not included in this paper, and (b) that those scattered X-ray photons only have marginal thermodynamic impact. Ly α do not deposit appreciable amount of energy into the system, neither do they destroy H₂ or CO. They do dissociate H₂O and OH, which can be important coolants. Nevertheless, with our numerical experiments, the soft FUV photons have the same effect but will likely penetrate deeper. We will revisit the Ly α scatter problem after obtaining the distribution of neutral hydrogen by simulations.³

Photons of those representative energy bins are traced by non-radial rays in curve-linear coordinates for the radiative transfer problem (L. Wang 2017, in preparation). For photochemistry, we must calculate the local effective flux for each cell,

$$F_{\text{eff}}(\nu) = \sum_{\{i \text{ in cell}\}} F_i(\nu) \left\{ \frac{1 - \exp[-\delta l_i/\lambda(\nu)]}{\delta l_i/\lambda(\nu)} \right\}, \quad (15)$$

where F_i is the incoming flux on the cell boundary carried by the i th ray, δl_i is the chord length of the ray crossing the cell, and $\lambda(\nu)$ is the mean free path of photons at frequency ν with all absorption mechanisms taken into

³ Ly α cooling is still included in our simulations (§4.3; see also WG17).

account, updated along with the evolution of chemical reaction network. The flux of a ray in each energy bin is also adjusted as it propagates through each cell according to the photochemical reactions and absorption processes within that cell.

4.3. Thermochemistry

In each cell of the simulation domain, the thermochemical reaction network is evolved in conjunction with hydrodynamics, in an operator-splitting manner (viz. hydrodynamics and thermochemistry are evolved in split steps, with the same step size in each cycle). A set of coupled ODEs are solved, reading nominally (note that the Einstein convention of summation is used),

$$\begin{aligned} \frac{dn^i}{dt} &= \mathcal{A}^i_{jk} n^j n^k + \mathcal{B}^i_j n^j ; \\ \frac{d\epsilon}{dt} &= \Gamma - \Lambda ; \end{aligned} \quad (16)$$

in which the terms involving $\{\mathcal{A}^i_{jk}\}$ describe two-body reactions, those in $\{\mathcal{B}^i_j\}$ represent photoionization, photodissociation, and spontaneous decays, and Γ and Λ represent the heating and cooling rates per unit volume, respectively. Stiff as they are, the ODEs of thermochemistry evolution can be solved with multi-step implicit method, which, by using the GPUs, is computed at costs comparable to the hydrodynamics (L. Wang 2017, in preparation).

As a direct product of planet formation that takes place in protoplanetary disks (PPDs), the *primordial* atmosphere of planets are expected to involve thermochemical processes similar to PPDs. We hence inherit the thermochemical network and recipes from WG17. Hereby we briefly summarize the thermochemical mechanisms involved and pertinent references:

- “Standard” two-body interactions in the UMIST database (McElroy et al. 2013; note that the photochemical reactions therein are not suitable for our radiation field, therefore they are excluded).
- Photoionization of atoms and molecules (Verner & Yakovlev 1995; Verner et al. 1996; photoionization of carbon atoms for FUV photons are subject to cross-shielding, see Tielens & Hollenbach 1985).
- Photodissociation of H_2 (subject to self-shielding, see Draine & Bertoldi 1996; note also that the FUV pumping of H_2 and subsequent reactions are also included, see discussions in Tielens & Hollenbach 1985), CO (subject to self-/cross-shielding, Visser et al. 2009), and H_2O (Ádámkóvics et al. 2014).
- Dust-assisted molecule formation (Bai & Goodman 2009; Ádámkóvics et al. 2014) and recombination (Draine & Sutin 1987; Weingartner & Draine 2001; see also the compilation in Ilgner & Nelson 2006).
- Photoelectric effects of dusts (Li & Draine 2001; Weingartner & Draine 2001).
- Dust-gas heat accommodation (Goldsmith 2001; Draine 2011).

TABLE 1
PROPERTIES OF THE FIDUCIAL MODEL

Item	Value
Radial domain	$r_{\text{in}} \leq r \leq 10 r_{\text{in}}$ ($r_{\text{in}} \simeq 2.448 R_{\oplus}$)
Latitudinal domain	$0 \leq \theta \leq \pi$
Resolution	$N_{\log r} = 128, N_{\theta} = 128$
Planet core	
M_c	$5 M_{\oplus}$
R_c	$1.495 R_{\oplus}$
Planet Atmosphere	
M_{ad}	$10^{-2} M_c$
T_{eq}	886 K
τ_{KH}	10^8 yr
Radiation flux [photon $\text{cm}^{-2} \text{s}^{-1}$]	
7 eV (Soft FUV)	2×10^{15}
12 eV (LW)	5×10^{13}
25 eV (EUV)	5×10^{14}
1 keV (X-ray)	1.3×10^{13}
Initial abundances [n_X/n_{H}]	
H_2	0.5
He	0.1
H_2O	1.8×10^{-4}
CO	1.4×10^{-4}
S	2.8×10^{-5}
Si	1.7×10^{-6}
Fe	1.7×10^{-7}
Gr	1.0×10^{-7}
Dust/PAH properties	
r_{dust}	5 \AA
ρ_{dust}	2.25 g cm^{-3}
$m_{\text{dust}}/m_{\text{gas}}$	7×10^{-5}
σ_{dust}/H	$8 \times 10^{22} \text{ cm}^2$

- Atomic cooling (Tielens & Hollenbach 1985; for escape probability see Kwan & Krolik 1981).
- Ro-vibrational cooling of molecules (Neufeld & Kaufman 1993; Omukai et al. 2010).

5. FIDUCIAL MODEL

In this section we describe the setup and results of the fiducial model, which is the reference point of all further numerical explorations. The main properties of our fiducial model is summarized in Table 1.

5.1. Fiducial model setup

We setup the simulation in an axisymmetric spherical polar grid; dependence on the azimuthal coordinate (ϕ) is ignored. The symmetry axis points to the host star, from which the radiation comes as parallel rays. The grid extends from r_{in} to $10 r_{\text{in}}$ in radius (r) and 0 to π in co-latitude (θ). r_{in} is defined as the radius at which the static density equals to a reference value ρ_{in} , which can be smaller than ρ_{rcb} since photoevaporation only affects the outermost part of isothermal layer. In this paper we choose $\rho_{\text{in}} = 10^{-7} \text{ g cm}^{-3}$ unless specifically noted. For the fiducial model, $r_{\text{in}} = 2.448 R_{\oplus}$, which guarantees that all relevant dynamical, radiative and thermochemical processes are taking places inside the simulated do-

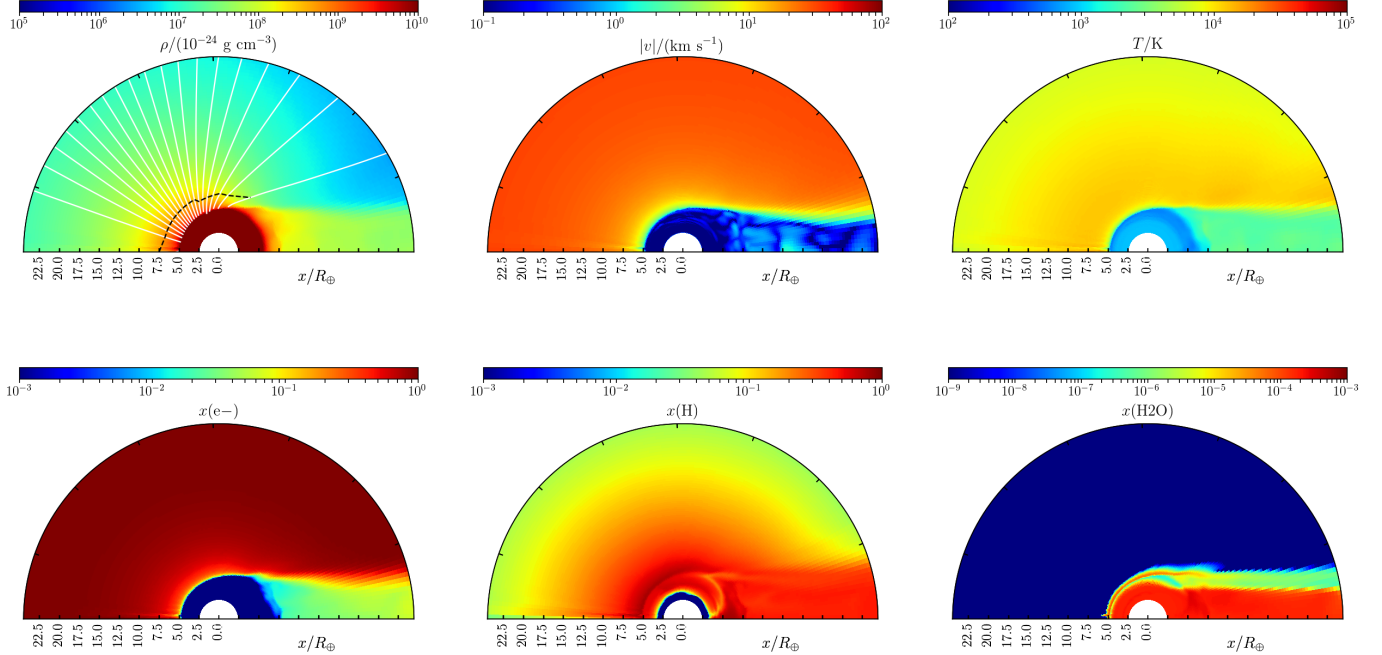


FIG. 3.— Meridional slice plot of the fiducial model at steady state, averaged through the final 0.05 yr of the fiducial simulation. The top row presents fluid properties, including mass density ρ (upper left panel; colormap saturated for $\rho > 10^{-10}$ g cm $^{-3}$ to present the wind better), magnitude of velocity $|v|$ (upper middle), and temperature T (upper right). The bottom row exhibits the relative abundances of important chemical species, including electrons (lower left), neutral hydrogen (lower middle), and water (lower right). The streamlines (white solid curves; separated by 2×10^{-11} M_{\oplus} yr $^{-1}$ mass loss rate) and transonic surface (black dashed curve) are overlaid in the density panel. Regarding the way of presentation in this figure, rays for radiative transfer are injected from the left, and all rays travel horizontally across the simulation domain. Note the hydrostatic “tail” on the right side over the planet; see §5.2.3.

main.⁴ Outflow boundary conditions with a radial flow limiter are imposed at $r = 10 r_{\text{in}}$, and reflecting boundary conditions at $r = r_{\text{in}}$, while $\theta = 0$ and $\theta = \pi$ are polar boundaries. The resolution is 128 radial by 128 latitudinal; the radial zones being logarithmically spaced, and the latitudinal zones equally spaced. Rays of high energy radiation are injected at the $r = 10 r_{\text{in}}$ boundary in the θ range $0 < \theta < \pi/2$, carrying uniform flux density in each energy bin. All rays are parallel to the symmetric axis.

The fiducial model has a $M_c = 5 M_{\oplus}$ rocky core, whose radius is therefore $R_c \simeq 1.495 R_{\oplus}$ (see §2). The gravitational field is set according to the core; self-gravity of the atmosphere is ignored. Outside the core, we set an adiabatic envelope with $M_{\text{ad}} = 10^{-2} M_c$, surrounded by an isothermal layer characterized by $T_{\text{eq}} = 886$ K (eq. 1). The initial density profile is set according to the discussions in §2, with $\tau_{\text{KH}} = 10^8$ yr (see eq. 9). This fiducial model has $\beta_{\text{ad}} = 3.94$ and $\rho_{\text{rcb}} = 1.1 \times 10^{-2}$ g cm $^{-3}$. The specific entropy in the adiabatic atmosphere is $\sim 8.3 k_B$ per baryon.

Host star luminosities in high energy photon are calibrated as $L_{\text{EUV}} + L_X = 10^{30}$ erg s $^{-1}$ (e.g. Owen & Jackson 2012; OW17). In each energy bin the luminosity is set according to the $t < 0.1$ Gyr SED concluded in Ribas et al. (2005), which approximately reads $L(7 \text{ eV}) = L(25 \text{ eV}) = L(1 \text{ keV}) = 0.5 \times 10^{30}$ erg s $^{-1}$, and $L(12 \text{ eV}) = 0.5 \times 10^{29}$ erg s $^{-1}$. Those luminosities

⁴ For the fiducial model, we vary the value of ρ_{in} by ± 1 orders of magnitude for different r_{in} , to confirm that the mass loss rate is invariant up to $\sim 5\%$.

are converted into fluxes at $a = 0.1$ AU, assuming that the stellar radiation is isotropic. The initial abundance of chemicals is the same as WG17, which is a subset of Gorti & Hollenbach (2008), defined by the values in Table 1 (where n_{H} is the number density of hydrogen nuclei).

Dust (including PAH) is one of the most important mechanisms that maintain the temperature in the isothermal region: in optical and infrared bands where the radiation from the central star is most energetic, dusts provide most of the opacity. The abundances of PAH in exoplanet atmospheres, however, are still unconstrained due to difficulties in observation. Observations within the solar system suggest that relatively high concentration of PAH is possible (e.g. López-Puertas et al. 2013 shows that the mass fraction in PAH is $\sim 2 \times 10^{-3}$ in the fully evolved nitrogen-rich atmosphere of Titan, with ~ 34 carbon atoms per PAH particle on average). Similar to WG17, we use the PAH at 5 Å as a proxy of all dusts, with abundance 10^{-7} per hydrogen atom. The dust-to-gas mass ratio is then 0.7×10^{-4} , and $\sigma_{\text{dust}}/\text{H} = 8 \times 10^{22}$ cm 2 for the geometric cross section. Instead of calculating the radiative transfer of optical and infrared radiation, we set the dust temperature $T_{\text{dust}} = T_{\text{eq}}$ everywhere in the simulation for simplicity. The emission power per dust surface area is proportional to approximately the sixth power of dust temperature considering dust emissivity (see e.g. Draine 2011); slight deviation of T_{dust} from T_{eq} will result in rapid restoration of T_{dust} back to T_{eq} .

The fiducial model is run through $\sim 10^{-1}$ yr to guarantee that the system reaches quasi-steady state, especially that the photospheres of high energy radiation in

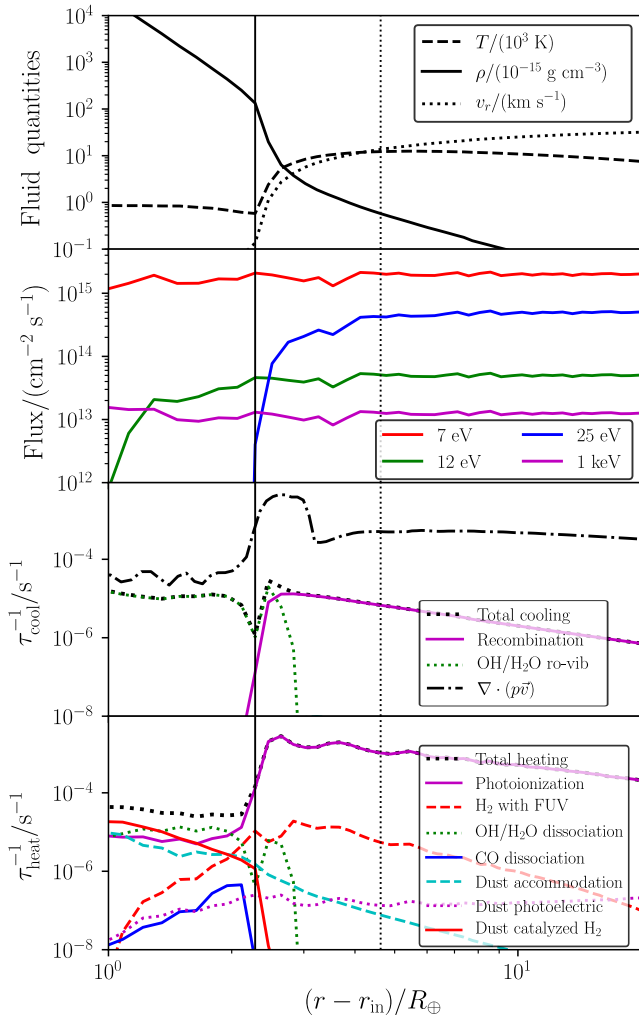


FIG. 4.— Radial profiles at $\theta = 0.4$ of the time-averaged fiducial model. Fluid mechanics profiles (ρ , v_r and T , upper left panel), radiation flux in four energy bins (lower left), inverse cooling timescale (τ_{cool}^{-1} , upper right), and inverse heating timescale (τ_{heat}^{-1} , lower right) in four panels, respectively. Denotation of curve shapes and colors are indicated in each individual panel. Vertical solid lines show the wind base, while vertical dotted lines indicate the sonic point.

four bins do not move. We confirm that the system is already steady after only $\sim 5 \times 10^{-3}$ yr: the dynamical timescale across the simulation domain is at the order of $t_{\text{dyn}} \sim 40 R_{\oplus}/v_r \sim 10^{-4}$ yr, and the quasi-steady state is established after only a few t_{dyn} .

5.2. Fiducial model results

The meridional plots, showing the structure of the fiducial model in the quasi-steady state, are displayed in Figure 3. The flow structure is shown by white streamlines overlaid on the mass density panel (upper left), separated by constant mass loss rate $2 \times 10^{-11} M_{\oplus} \text{ yr}^{-1}$ (integrated through the polar and azimuthal region between neighbor streamlines). Streamlines are only plotted in regions with positive “Bernoulli parameter”, defined as

$$\mathcal{B} \equiv \frac{v^2}{2} + \frac{\gamma p}{(\gamma - 1)\rho} + \Phi, \quad (17)$$

TABLE 2
CHARACTERISTIC RADII OF THE FIDUCIAL MODEL

Item	Value
R_c/R_{\oplus}	1.50
$r_{\text{rcb}}/R_{\oplus}$	1.91
r_{in}/R_{\oplus}	2.45
$R_{\text{EUV}}/R_{\oplus}$	4.78
R_s/R_{\oplus}	7.24

NOTE. — The fiducial model is defined in Table 1.

where v is the magnitude of velocity vector, and Φ is the gravitational potential. The surface where the streamlines terminate is considered as the base of photoevaporation outflow, which is located at $r \simeq 5 R_{\oplus}$. In Table 2 we present several radii as characteristic locations of different physical processes. Note that R_{EUV} is the radius of EUV photosphere, defined as where F_{EUV} drops to 10^{-2} of the unattenuated value, which also defines the wind base in our following analyses.⁵

5.2.1. Radial profiles of thermodynamics

Along a typical radial column at co-latitude $\theta = 0.4$ (where the streamline is almost radial), the hydrodynamical and microphysical profiles are shown in Figure 4. Only important mechanisms of heating and cooling are included in the lower two panels, where the inverses of heating/cooling timescales are defined as internal energy density divided by the cooling/heating rate, $\tau_{\text{cool,heat}}^{-1} \equiv \epsilon/f(\text{cool, heat})$ (ϵ is the internal energy density of the gas; not to be confused with the Kelvin-Helmholtz timescale in 2.2). The term $\nabla \cdot (p\vec{v})$, as another kind of “cooling”, consists of adiabatic expansion and radial acceleration and characterizes the rate at which thermal energy is converted into kinetic energy. The heating curve marked by “H₂ with FUV” includes photodissociation and FUV pumping processes by LW FUV photons (see also §4.3).

Below the wind base, there is a small dip in temperature, thanks to dramatic expansion as the gas is accelerated. Inside the isothermal layer where EUV photons cannot reach, $|\nabla \cdot (p\vec{v})|$ of the gas creeping outwards at relatively very high density and very slow speed consumes the majority of injected energy, at a rate about three times the dissipation by ro-vibrational cooling of H₂O and OH. Spatial locations of the peaks in cooling rate by H₂O/OH agree with the spatial distribution of water molecules (see Figure 3). Note that there is a layer of H₂O detached to the bulky molecular atmosphere, where the re-formation rate of H₂O exceeds the photodissociation and thermal collisional destruction rate. Cooling mechanisms via recombination and Ly α , in contrast, are negligible. On the heating side, photoionization brought by X-ray and LW photons, photodissociation of H₂O and OH, re-formation of H₂ on dust surface, and photoelectric effect of dust grains, are the four comparable mechanisms that are major heating sources.

From the profiles presented by Figure 3, we observe that the day hemisphere has a clear outflow above the isothermal layer. The outflow becomes supersonic at the black dashed curve (marking the sonic points), which

⁵ by numerical experiments, we find that this criteria result in an almost invariant ρ at R_{EUV} for different physical parameters.

confirms that it is a wind rather than a “breeze”. As is seen in Figure 4, in the subsonic part of wind, the thermodynamics of gas is dominated by photoionization and $\nabla \cdot (p\vec{v})$. Beyond the sonic point, radial acceleration almost vanishes, and $|\nabla \cdot (p\vec{v})|$ gradually surpasses photoionization heating, which causes a slight decrease in temperature.

5.2.2. Neutral hydrogen and planet size in Ly α

We notice that neutral hydrogen atmos still exist at a considerable fraction in the wind, thanks to the capability of dealing with non-equilibrium thermochemical processes⁶. The timescale of hydrogen photoionization is roughly $(F_{\text{EUV}}\sigma)^{-1} \sim 0.5$ hr, allowing a fluid element in the wind to travel $\sim 8.4 R_{\oplus}$ before its fraction of neutral hydrogen decreases by one e-fold. The low ionization fraction prohibits the propagation of Ly α into the isothermal layer: the line-center optical depth is $\sim 10^{6-7}$, which allows us to ignore Ly α radiative transfer safely. Meanwhile, neutral hydrogen in the wind makes the observed size of planet in Ly α much bigger than other bands. The dimensionless equivalent width on a wide Ly α profile denoted by $\phi(u)$, is estimated as (here u is the line-of-sight velocity),

$$W = \left[\int du \phi(u) \right]^{-1} \times \left[\int du \phi(u)(1 - e^{-\tau(u)}) \right]. \quad (18)$$

We assume that $\phi(u)$ is a Gaussian profile with FWHM ~ 200 km s⁻¹, and that $\tau(u)$ is another Gaussian with FWHM ~ 50 km s⁻¹, combining the bulk and thermal motion of the outflow. By integrating τ and then W along different lines of sight, we find that $W \sim (1 - e^{-1})$ at an impact parameter $b \sim 11 R_{\oplus}$, which roughly indicates the observed size in Ly α during transits. The excess of observed size of planets in Ly α compared to optical is readily observed in Jupiter-size objects (e.g. Lecavelier Des Etangs et al. 2010). According to our simulations, the same holds true for sub-Neptune planets.

5.2.3. Flow structures and the mass loss rate

Above the night hemisphere, where no high energy photons can ever reach, there exists a roughly isothermal “tail” at $\rho \sim 10^{-15} - 10^{-16}$ g cm⁻³ and $T \sim 2 \times 10^3$ K. The tail is almost static; the velocity magnitude is roughly below 10^{-1} km s⁻¹. The streamline structures and the evolution history both reveal that the tail is brought about by the gas flowing along the streamline originating from $\theta \simeq \pi/2$, similar to the Bernoulli effect for isenthalpic flows. Existing works of planet atmosphere suggest much larger tails (outside the Roche lobe of the planet) which are typically attributed to ram pressure of stellar wind or radiation pressure of the central star (e.g. Christie et al. 2016; Bourrier et al. 2016), while the tail here comes from the thermal wind of the planet itself. The fate of this “smaller” tail, however, has to be studied with full three-dimensional simulations in order to include the effects of planet orbital motion, which we will tackle in an upcoming paper.

⁶ We confirm that the existence of neutral hydrogen in the wind does not affect the structure of photoevaporating atmosphere by a test run, whose outer boundary is set at $r = 10^2 r_{\text{in}}$ and the radial number of zones is doubled so that the mesh configuration in the innermost 10 r_{in} is identical to the fiducial run.

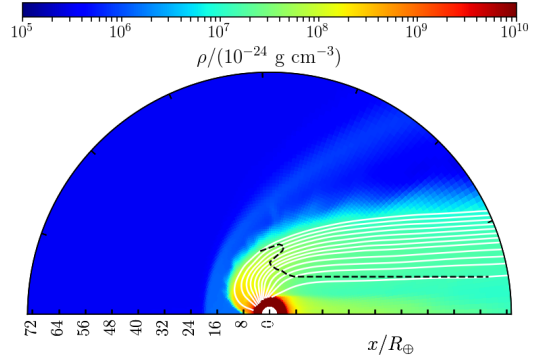


FIG. 5.— Meridional slice plot of the $p_{\text{ram}} = 10^{-3}$ dyn cm⁻² case in Models W, where a strong stellar wind ram pressure is included. The colormap exhibits the mass density ρ , showing the time-averaged results for the final 10^{-2} yr. The denotation of overlays in this figure are identical to the upper left panel of Figure 3. See §6.1 for the details of simulation setup. ^a

^aAn animation showing the evolution of this model is available as online supplement material

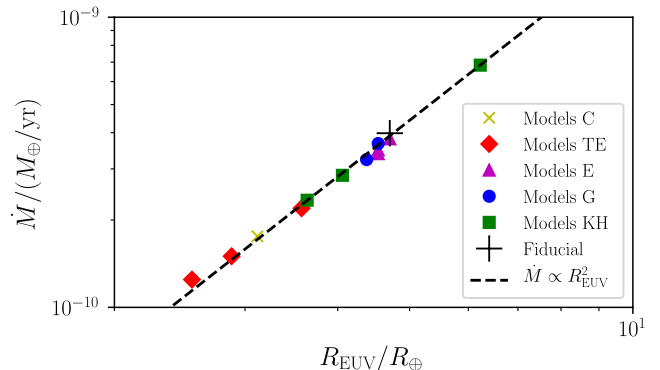


FIG. 6.— Scattered plots showing the \dot{M} - R_{EUV} relations for Models E, G, KH, TE, and C, as well as the fiducial model. Makers of each model series are indicated by the legend. The simple relation $\dot{M} \propto R_{\text{EUV}}^2$ is shown by a dashed line.

By integrating the mass flux through the outer boundary of r , we obtain a mass loss rate $\dot{M} \simeq 4 \times 10^{-10} M_{\oplus} \text{ yr}^{-1}$. For the fiducial case alone, multidimensionality does not contribute to the mass loss rate appreciably. Multiplying the radial mass flux at $\theta = 0$ (at the substellar point) by 2π (the solid angle of day hemisphere), the estimated mass loss rate is only $\sim 3\%$ bigger than the value measured from simulation. The dimensional effects (i.e. 2.5 dimensions with axisymmetry) are nonetheless manifested by models with strong stellar wind ram pressure (see §6.1).

6. EXPLORING THE PARAMETER SPACE

We have run serieses of simulations to explore the effects of different parameters. To manifest the impact of each parameter more clearly, each run in this subsection differs from the fiducial model by only one parameter unless specifically stated. Table 3 lists the model serieses [indicated by “Model(s) Y” for the model series Y in what follows] with brief descriptions.

6.1. Stellar wind ram pressure and the effects of multidimensions

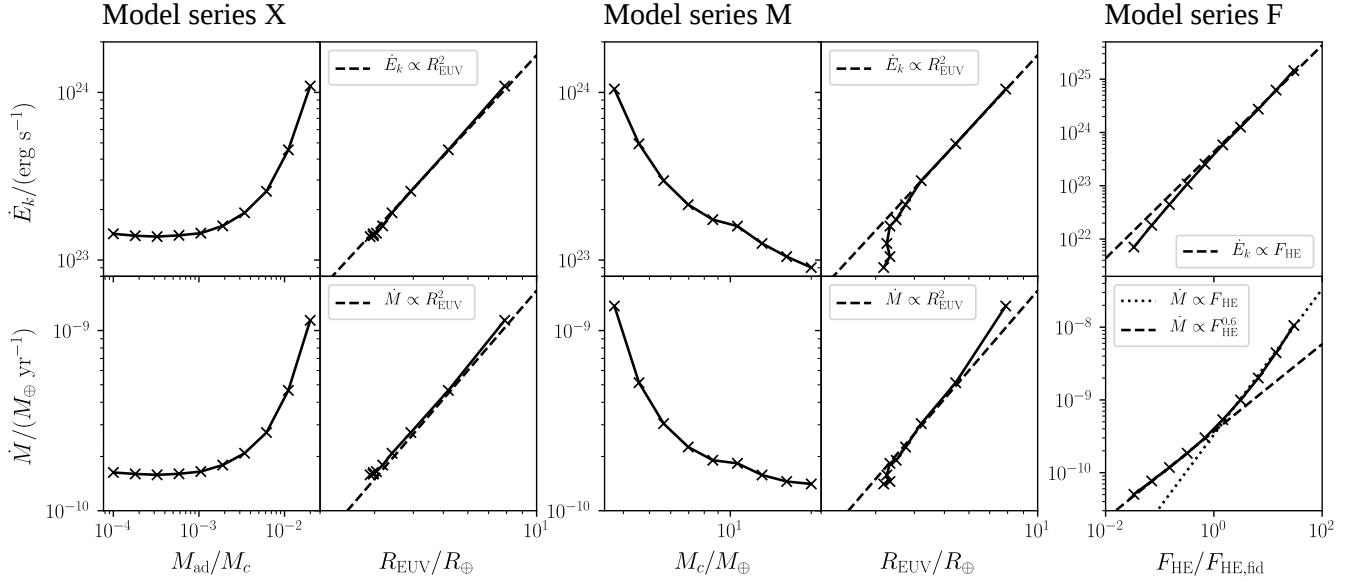


FIG. 7.— Simulation results of model series X (varying envelope mass fraction; left block), M (varying core mass; central block), and F (varying high energy flux, right block). Each data point, representing a model in its quasi-steady state, is indicated by a cross (“×”). In some panels, dashed or dotted lines present simple power-laws (indicated by legends in the panels) to help the reader recognize the general trend of variation. Panels related to R_{EUV} are not shown for model series F as R_{EUV} does not vary appreciably in the series. y -axes of the panels on the top-row all present \dot{E}_k (the kinetic energy carried by the outflow, in erg s^{-1}), while those of the bottom-row panels present \dot{M} (the mass loss rate, in $M_\oplus \text{ yr}^{-1}$).

TABLE 3
MODELS EXPLORING THE PARAMETER SPACE

Model Series	Variable	Values
(1)	(2)	(3)
Microphysics parameters		
E	Energy bin turned off (eV)	{7, 12, 25, 10 ³ }
G	Dust grain abundance	{10 ⁻⁸ , 10 ⁻⁹ }
Atmosphere parameters		
KH	$\tau_{\text{KH}}/(10^8 \text{ yr})$	{0.3, 3, 10}
TE	T_{eq}/K	{411, 518, 703}
X	M_{ad}/M_c	[10 ⁻⁴ , 0.02]
Planet and stellar properties		
W [†]	$p_{\text{ram}}/(\text{dyn cm}^{-2})$	{10 ⁻⁴ , 10 ⁻³ , 10 ⁻² }
C	Core composition	{Iron, Water}
M	M_c	[3, 20]
F	Relative high energy flux	[1/30, 30]

NOTE. — (1) Model series identifier. (2) Description of the varied quantity in the model series. (3) Sets of values of the variable. Squared brackets $[l, u]$ denote that the variable will take several different values between lower limit l and upper limit u , while braces “{ }” indicate that the variable will select one of the discrete values in the braces at a time.

†: See §6.1 for details of simulation setup.

For a typical radial column above the day hemisphere, in which the flow is virtually radial, we derive the total pressure of outflow (including thermal pressure and fluid ram pressure), from conservation of momentum (here $v_{r,\infty}$ is the terminal radial velocity of outflows),

$$p_{\text{tot}} \simeq 10^{-3} \text{ dyn cm}^{-2} \times \left(\frac{\dot{M}}{10^{-10} M_\oplus \text{ yr}^{-1}} \right) \times \left(\frac{v_{r,\infty}}{34 \text{ km s}^{-1}} \right) \left(\frac{r}{5 R_\oplus} \right)^{-2}. \quad (19)$$

This pressure is typically much greater than ambient pressure (eq. 6), which allows us to safely ignore the ambient constraints once photoevaporation outflow is launched. If the model is 1D and spherical symmetric, when the ram pressure exerted by the stellar wind p_{ram} is comparable to the total pressure near the sonic point (namely $p_{\text{tot},s}$), one would expect that the supersonic outflow is quenched while only a subsonic breeze is possible (see also M-CCM09).

However, considering the multidimensional reality, it is more likely that the supersonic planetary winds would divert to the night hemisphere instead of being totally choked. We hence compute simulation Models W, in which we setup significant inflow at the outer r -boundary, in the range $0 < \theta < \pi/2$ (the boundary condition is the same as fiducial in $\pi/2 < \theta < \pi$). The inflow is parallel to the radiation fluxes, at velocity $v = 500 \text{ km s}^{-1}$, and temperature $T = 10^5 \text{ K}$. Mass density of the inflow is the variable that controls p_{ram} in Models W: $\rho = 4 \times 10^{-19} \text{ g cm}^{-3} \times (p_{\text{ram}}/10^{-3} \text{ dyn cm}^{-2})$. Three different ram pressures are tested respectively, $(p_{\text{ram}}/\text{dyn cm}^{-2}) \in \{10^{-4}, 10^{-3}, 10^{-2}\}$, compared to the total outflow pressure at the sonic point $p_{\text{tot},s} \simeq 1.8 \times 10^{-3} \text{ dyn cm}^{-2}$ for the fiducial model. The outer boundary is $30 r_{\text{in}}$ so that all important hydrodynamic features are correctly included in the simulation domain, and the number of radial zones is adjusted accordingly in order to keep the resolution of the innermost region identical to the fiducial one.

In their quasi-steady states, all cases in Models W still have significant supersonic outflows originating from the day hemisphere flowing to the night side. Although the flow morphology changed dramatically, the mass loss rate is comparable to the fiducial model. Previous one-dimensional calculations carried out by M-CCM09 could not capture the multidimensional effects, thus incorrectly predicted the quenching of supersonic photoevaporative

outflow when ram pressure becomes significant. For each individual model:

- The $p_{\text{ram}} = 10^{-3}$ dyn cm $^{-2}$ case has mass loss rate $\dot{M} \simeq (3.0 \pm 1.1) M_{\oplus} \text{ yr}^{-1}$ (the uncertainty here is the standard deviation over the final 10^{-2} yr, reflecting the variation amplitude of the outflow). In Figure 5, we present a meridional plot of mass density with streamlines overlaid for this case, based on the time-averaged results during the final quasi-steady state (10^{-2} yr) of the simulation. Although the outflows are suppressed by the post-shock external wind near the substellar point, they still find their ways out on the night side and become supersonic. The discontinuity surface is rather turbulent thanks to Kelvin-Helmholtz instability (as the fluid speed behind the bow shock is still $\sim 10^2$ km s $^{-1}$), which in turn affects the shape of the shock as the post-shock flow is subsonic. Therefore we do not observe sharp transitions for the bow shock and the discontinuity in Figure 5.
- The $p_{\text{ram}} = 10^{-4}$ dyn cm $^{-2}$ case also has turbulent supersonic outflow, with mass loss rate $\dot{M} \simeq (3.3 \pm 1.0) M_{\oplus} \text{ yr}^{-1}$.
- The test case $p_{\text{ram}} = 10^{-2}$ dyn cm $^{-2}$ still has $\dot{M} \simeq (3.1 \pm 0.1) M_{\oplus} \text{ yr}^{-1}$ mass loss rate, even when the ram pressure is one order of magnitude greater than the fiducial total pressure at the sonic surface $p_{\text{tot},s}$. The supersonic outflow becomes fairly laminar in this case.

6.2. Different bands of radiation

Models E, varying the SED of incident high energy radiation by turning off one band of radiation at a time, help us to understand in which band is the high energy photons most relevant to photoevaporation. Simulation results reveal that only the EUV photons have primary impact on the mass loss rate. By turning off the EUV flux, the mass loss rate drops to $\dot{M} \lesssim 10^{-12} M_{\oplus} \text{ yr}^{-1}$, while the gas is creeping outwards at a radial velocity $v_r \lesssim 10^{-1}$ km s $^{-1}$. This is understood by comparing the depth of gravitational potential well, which is roughly ~ 1 eV per proton for a $5 M_{\oplus}$ planet core at $r \sim 3 R_{\oplus}$, to the energy per particle deposited by high energy photons.

When an EUV photon is absorbed by a hydrogen atom/molecule, photoionization processes deposit roughly 10 eV per reaction of energy to the post-interaction particle. LW photons, in comparison, deposit only ~ 0.5 eV of energy into each hydrogen atom by dissociating a H $_2$ molecule (e.g. Hollenbach & McKee 1979), which is marginally sufficient to free it from the potential well. As EUV photons interact with the most abundant elements (hydrogen and helium), the energy injected is not considerably diluted. In contrast, energy injected by soft FUV and X-ray photons, which interact predominantly with species at relatively low abundance (especially water and dust grains), experiences significant dilution. Soft FUV and X-ray photons penetrate to higher depths where the number densities of hydrogen nuclei are rather high ($\sim 1 \times 10^{14}$ cm $^{-3}$ for soft FUV and $\sim 3 \times 10^{14}$ cm $^{-3}$ for X-ray). At those

high densities, energy deposited by those photons is easily transferred to coolants or accommodated by dusts, and then re-radiated as infrared photons that are not efficient in heating the gas at all.

Meanwhile, when bands other than EUV are turned off, the mass loss rate is only secondarily affected: being responsible to modifying the temperature in quasi-isothermal layer, turning off a non-EUV band of radiation leads to (a) slight shrinking of the quasi-isothermal layer and hence EUV photosphere, and (b) survival of more coolants. As a result, the mass loss rate decreases by $\sim 5\%$ (LW off) or $\sim 15\%$ (X-ray or soft FUV off).

6.3. Configuration of atmospheres

An important substance maintaining temperature in the isothermal layer as they are, dust grains (which we use PAH as the proxy) have nonetheless highly uncertain abundances (see §5.1). In Models G, we confirm that the abundance of Gr affects \dot{M} by competing with the cooling mechanisms in the quasi-isothermal region and then setup the location and structure at the EUV photosphere. Reducing the Gr abundance by one or two orders of magnitude results in a $\sim 10\%$ or $\sim 20\%$ decrease in \dot{M} respectively.

Covering the uncertainties in the hydrostatics of planet atmosphere, we setup Models KH and TE. τ_{KH} and T_{eq} together characterize the specific entropy and hence the density profile of the atmosphere (see §2.2). Models C, varying the core density by assuming an iron or water core below the atmosphere (using the mass-radius relation in Lopez & Fortney 2014 for different core components), also modify the atmospheric density profile dramatically.

It is worth noting that almost all models discussed above obey the simple relation, $\dot{M} \propto R_{\text{EUV}}^2$, as R_{EUV}^2 is proportional to the effective area for the planet to intercept EUV photons. We exhibit this scaling relation in Figure 6.

6.4. Envelope mass fraction and the planet core

Models X, varying the envelope mass fraction, also clearly presents the dependence $\dot{M} \propto R_{\text{EUV}}^2$, as is seen in the left column in Figure 7. This relation is almost invariant when the wind starts from different depth in the gravitational potential well: the kinetic energy at $v_{\text{wind}} \simeq 32$ km s $^{-1}$ overwhelms the gravitational potential (escape velocity is only ~ 11 km s $^{-1}$ at $r = 5 R_{\oplus}$ for a $5 M_{\oplus}$ core) and other energy balance as a fluid element escapes. The kinetic energy carried by the outflow, \dot{E}_k , also follows the same proportionality. Thermal energy carried by the outflow is only $\sim 10^{-1}$ of \dot{E}_k , hence does not affect our discussions.

When the core mass varies in the Models M, the physics becomes slightly different (see the middle column in Figure 7). If $M_c \gtrsim 10 M_{\oplus}$, R_{EUV} varies much slower with M_c , but the depth of the potential well starts to become significant. In the hypothetical case with $M_c = 20 M_{\oplus}$, $v_{r,\infty}$ drops to ~ 26 km s $^{-1}$, as the gas spent part of its energy against gravitational potential well when escaping.

6.5. High energy photon flux and “cooling limited”

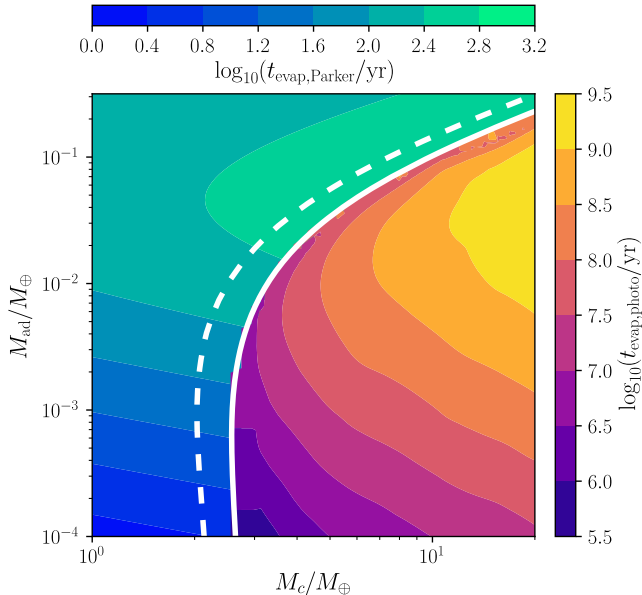


FIG. 8.— Evaporation timescale of planet atmosphere. The heavy white curve is the critical curve above which the isothermal layer pressure cannot be balanced by the ambient ($p_\infty < p_{\text{amb}}$, see §2.3), and the white dashed curve indicates $\rho_\infty \simeq 10^{-13} \text{ g cm}^{-3}$, above which the pressure balance by outflow is no longer valid (see also discussions in §7.1). t_{evap} in the region with unbalanced ambient pressure above the solid white curve is calculated with eqs. (11) and (12), which should read the blue-green color map indicated on the top. t_{evap} based on simulation results, presented by the region below the critical curve, should read the purple-yellow color map on the right.

In Models F (see the right column in Figure 17), R_{EUV} does not vary appreciably with the luminosity. When the high energy fluxes are weak ($F_{\text{HE}} \lesssim F_{\text{HE, fid}}$), the mass loss rate scales as $\dot{M} \propto F_{\text{HE}}^{0.6}$ (shallower than linear), while the kinetic energy of outflow drops faster than linear. Considering the proportionalities $\dot{M} \propto r^2 \rho v_r$ and $\dot{E} \propto r^2 \rho v_r^3$, this clearly indicates that the outflow speed drops drastically at low luminosities, which in turn increases the efficiency of converting energy into outflow. In fact, for $F_{\text{HE}}/F_{\text{HE, fid}} = 1/30$, we have $v_{r, \infty} \simeq 12 \text{ km s}^{-1}$. At high fluxes, \dot{M} has linear dependence on F_{HE}

Interestingly, M-CCM09 claimed that $\dot{M} \propto F_{\text{HE}}^{0.6}$ at high F_{HE} due to increasing rate of recombination cooling, and that $\dot{M} \propto F_{\text{HE}}^{0.9}$ otherwise. They concluded that recombination cooling at high F_{HE} is the limiting factor (“recombination limited”). Our models confirmed the power index 0.6 when cooling is the major limit. However, involving detailed thermochemistry reveals that the dominant coolants are the molecules via ro-vibrational transitions, while recombination is indeed impossible to remove injected heat at considerable amounts near the wind base (see discussions in §3.2). At lower F_{HE} , the abundances of molecular coolants are higher. We hence summarize the mass loss rate at low F_{HE} with a more general term, “cooling limited”, instead.

7. DISCUSSIONS

7.1. Grid data of photoevaporative model and evaporation timescale

In order to understand the general trend of t_{evap} varying with different planet configurations, we run a grid of simulations with parameters in the space where $p_\infty <$

p_{amb} (parameters unspecified are identical to the fiducial model),

$$\begin{aligned} & \{M_c/M_\oplus, M_{\text{ad}}/M, F_{\text{HE}}/F_{\text{HE, fid}}\} \\ & \in \{[3, 20] \otimes [10^{-4}, 10^{-0.5}] \otimes [10^{-2}, 1]\} \cap \{p_\infty < p_{\text{amb}}\}. \end{aligned} \quad (20)$$

The resolution is 10 logarithmically-spaced grid points along M_c , 10 logarithmic along M_{ad}/M_c , and 3 logarithmic along F_{HE} . After excluding $p_\infty > p_{\text{amb}}$ points 261 simulations in total have been integrated to at least $10^2 t_{\text{dyn}}$. Figure 8 plots t_{evap} the grid at $F_{\text{HE}}/F_{\text{HE, fid}} = 1$, where data in the region $p_\infty > p_{\text{amb}}$ (above the heavy white curve) present the timescale of mass loss through Parker wind (§2.3).

When the envelope of a planet starts evolution in the Parker wind region, it is expected to be dispersed rapidly, at timescale shorter than 10^3 yr , until it becomes a “bare” planet ($M_c \lesssim 3 M_\oplus$), or reaches the photoevaporation region ($M_c \gtrsim 3 M_\oplus$), as we already discussed in §2.3. This scenario is slightly changed when high energy radiation fluxes exist. Compared to the ambient, outflows exert much greater pressure confinement onto the internal static atmosphere at wind bases (see eq. 19). However, this kind of “confinement” does require the isothermal atmosphere to allow EUV photons penetrate. Inspecting the location of EUV photosphere in various models, R_{EUV} is always found at radii where $\rho \sim 10^{-13} \text{ g cm}^{-3}$ (also see discussions in M-CCM09); if $\rho_\infty \gtrsim 10^{-13} \text{ g cm}^{-3}$, EUV photons are unlikely to penetrate, and this mechanism (pressure balance by outflow) is not valid either. In Figure 8 we present this criterion by a white dashed curve. The region between two type of pressure balancing is rather narrow. Therefore, in practice, adopting the ambient pressure balancing criterion will not significantly change the story, which is what we will do in the followings.

Planets in the photoevaporative domain disperse their envelopes at much longer timescales. In particular, the timescale peaks at $M_{\text{ad}}/M_c \sim 10^{-2}$, $t_{\text{evap}} \gtrsim 10^8 \text{ yr}$ for $M_c \gtrsim 5 M_\oplus$. At the same M_c , planets with M_{ad}/M_c above this peak have rather puffy envelope, and R_{EUV}^2 increases dramatically faster than M_{ad} . The power injected by intercepting EUV photons per M_{ad} hence increases, shortening t_{evap} as a result. Below that peak, R_{EUV} does not shrink appreciably, especially when $M_{\text{ad}}/M_c \lesssim 10^{-3}$. \dot{M} is almost constant, thus $t_{\text{evap}} \propto M_{\text{ad}}$ becomes shorter and shorter as a planet loses its envelope mass. Qualitatively those are similar to the mechanisms proposed in OW17 which are probably responsible of the bimodal distribution of observed planet radius. We will discuss this with more details in §7.3. We particularly noticed that, for planets with core mass $M_c \lesssim 6 M_\oplus$, evaporation timescales of their envelopes will be shorter than $\sim 300 \text{ Myr}$ everywhere. In other words, under fiducial set of parameters, photoevaporation prevents us from finding rich H/He envelopes on those low mass planets in evolved systems. This is not a hard limit, since the photoevaporation conditions vary from system to system, while t_{evap} depends on those conditions rather sensitively. Nevertheless, observations show the decline in number of planets with rich atmospheres (see also Dressing et al. 2015; Rogers 2015). We thus suggest that this decrease

can be attributed to photoevaporation.

7.2. Scaling relations of the mass loss rate

Based on the simulation grid as well as the explorations in §6, in almost all cases already tested, the relation $\dot{M} \propto R_{\text{EUV}}^2$ holds very well (except for $M_c \gtrsim 10 M_\oplus$, where the depth of potential well begins to make a difference). We notice that, in M-CCM09 and OW17, the mass-loss rate is scaled to an expression proportional to r_{rcb}^3 . The third power implies two assumptions, if the efficiency is nearly constant:

1. Terminal specific energy of the outflow is proportional to the depth of gravitational potential well at the wind base.
2. The radius of EUV photosphere (approximately the same as wind base) is proportional to r_{rcb} .

Assumption 1 disagrees with our simulations, which indicate that the specific energy of outflow at infinity is almost invariant in most cases as it is much greater than the depth of potential well at wind bases. It is obvious that assumption 2 does not hold either. By observing our grid of photoevaporation models, we confirm that in each model R_{EUV} is always located at $\rho \sim 10^{-13} \text{ g cm}^{-3}$. Using eq. (5), we estimate by assuming that EUV photons penetrate to where $\rho \sim 10^{-13} \text{ g cm}^{-3}$,

$$R_{\text{EUV}} \simeq r_{\text{rcb}} \left[1 + \tilde{\beta}_{\text{iso}}^{-1} \ln \left(\frac{10^{-13} \text{ g cm}^{-3}}{\rho_{\text{rcb}}} \right) \right]^{-1}, \quad (21)$$

where r_{rcb} and ρ_{rcb} can be determined analytically using eqs. (3) and (10). Clearly $R_{\text{EUV}}/r_{\text{rcb}}$ is not constant. $\tilde{\beta}_{\text{iso}}$ here should be estimated using a different μ from the one used for the adiabatic layer, as hydrogen molecules in the upper part of the isothermal layer are partially dissociated by LW and X-ray photons. We find that $\mu \simeq 1.88 m_p$ fits R_{EUV} all models in the simulation grid and §6 with errors $\lesssim 10\%$ (mostly within 5%).

According to §6.5, the dependence of \dot{M} on incident high energy flux is linear if $F_{\text{EUV}} \gtrsim F_{\text{EUV,fd}}$, and $\dot{M} \propto F_{\text{EUV}}^{0.6}$ otherwise. Calibrated at the fiducial model, we propose a semi-empirical formula for mass loss rate that reads,

$$\begin{aligned} \dot{M} &\simeq 4.5 \times 10^{-10} M_\oplus \text{ yr}^{-1} \times \left(\frac{R_{\text{EUV}}}{5 R_\oplus} \right)^2 \\ &\times \max\{\mathcal{F}, \mathcal{F}^{0.6}\} \min\{1, \mathcal{M}^{-0.5}\}; \quad (22) \\ \mathcal{F} &\equiv \frac{F_{\text{EUV}}}{F_{\text{EUV,fd}}}; \quad \mathcal{M} \equiv \frac{M_c}{10 M_\oplus}. \end{aligned}$$

With R_{EUV} given by eq. (21), we test the mass loss rate fitting by setting up 100 simulations with random (but reasonable) combinations of all parameters, confirming that the error of eq. (22) is $\lesssim 20\%$ for most simulation runs, or $\lesssim 50\%$ at worst [most of the worst cases have relatively large R_{EUV} ($R_{\text{EUV}} \gtrsim 20 R_\oplus$) that cannot be accurately estimated by eq. (21)].

7.3. Mass and radius evolution of planet atmosphere

7.3.1. Evolution of sample planets

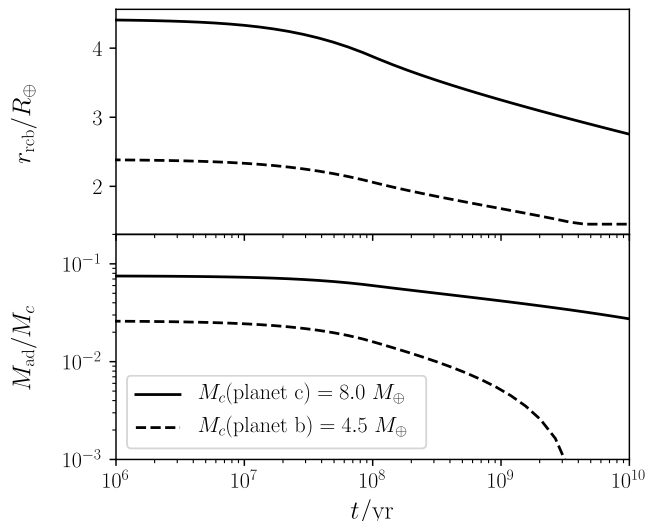


FIG. 9.— Evolution of model planet atmospheres, resembling the conditions of the two planets in Kepler-36, showing r_{rcb} and envelope mass fraction. Note that the two planets start from the same initial envelope mass fraction, but the less massive one (corresponding to Kepler-36b) has already evaporated most of its envelope via Parker wind before $t = 10^6$ yr. See §7.3.1 for detailed discussions.

Equipped with eqs. (22) and (21), we can model the evolution tracks of planet models by setting up initial conditions and then integrate the ODE $dM_{\text{ad}}/dt = \dot{M}$ for each model planet.

Figure 8 implies that, even the external conditions and the initial conditions are nearly the same, two planets would experience substantially different tracks of evolution if they have different core masses. Such systems are suggested by observations, but the most clear detection is Kepler-36, whose two planets circulate it at similar orbital radius (~ 0.12 AU) but have different core masses and observed radii (Kepler-36b: $4.5 M_\oplus$, $1.49 R_\oplus$; Kepler-36c: $8 M_\oplus$, $3.7 R_\oplus$; see also Carter et al. 2012). Here we setup two model planets according to Kepler-36. For other parameters, we set Kelvin-Helmholtz timescale $\tau_{\text{KH}} = 10^8 \text{ yr}$, isothermal layer temperature $T_{\text{eq}} = 850 \text{ K}$, and a evolving high energy luminosity with initial value one order of magnitude lower than the fiducial, $L_{\text{HE}}(t) = 10^{-4.5} L_\odot \times \min\{1, (t/10^8 \text{ yr})^{-1.5}\}$ (for the time-dependence see the discussions in §7.3.2). Both planets have initial envelope mass fraction $M_{\text{ad}}/M_c = 2 \times 10^{-1}$ (as both models will lose their atmosphere rapidly until they reach the pressure balance line, this parameter is not sensitively depended upon), and are integrated along the evolution tracks to 10^{10} yr . Figure 9 show their fate: at the age of Kepler-36, ($\sim 7 \text{ Gyr}$), the more massive planet still has a relatively rich atmosphere (M_{ad}/M_c is few per cent), while the other has already evaporated all its atmosphere. Considering the $\sim (+0.5 R_\oplus)$ correction applied to the more massive planet for the observed radius (given its r_{rcb} and core mass, e.g. Lopez & Fortney 2014), the bigger one should have $\sim 3.6 R_\oplus$ observed radius, while the other is a $\sim 1.5 R_\oplus$ “bare” planet. We thus conclude that the diverged evolution tracks due to photoevaporation agrees with observation semi-quantitatively (similar conclusion has also been reached by e.g. Lopez & Fortney 2013; Owen & Morton 2016).

7.3.2. Planet ensembles

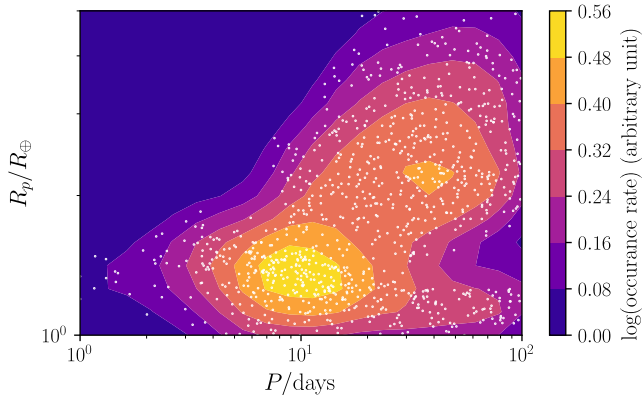


FIG. 10.— Bimodal distribution of evolved model planets. Scattered white dots present a sub-sample of simulated planet atmosphere evolution results (10^3 out of 10^4 ; for clearer presentation). The color-mapped contour is the estimated distribution function with Gaussian kernel, scaled to frequency per $\{\log_{10} P \times \log_{10} R_p\}$, using the results of the whole ensemble.

This subsection extends the calculation in §7.3.1 to a relatively big ensemble of planets. We start by setting up the initial and input conditions for the ensemble.

The distribution in orbital period is well-constrained by Kepler observations. We adopt the recipes of OW17, based on the observation results in Fressin et al. (2013), $dN/d \ln P \propto \min\{(P/7.6 \text{ days})^{1.9}, 1\}$, in the range $(P/\text{days}) \in [1, 10^2]$. The orbital periods are translated into orbital radii assuming the host stellar mass being M_\odot . At each orbital radius, T_{eq} and F_{HE} are set accordingly. The core mass distribution function is a Rayleigh function, $dN/dM_c \propto M_c \exp[-M_c^2/(2\sigma_M^2)]$ with $\sigma_M \sim 3 M_c$ and $(M_c/M_\oplus) \in [1, 12]$ (see also Marcy et al. 2014). We assume that the core of all model planets are rocky. The initial distribution of envelope mass fraction, however, is impossible to directly determine. We hence assume that the distribution function of $\ln(M_{\text{ad}}/M_c)$ is uniform in $(M_{\text{ad}}/M_c) \in [10^{-2}, 10^{-0.5}]$, and zero elsewhere. All those distributions are assumed to be independent to each other.

When evolving the planet envelopes, we integrate the mass loss process to 10^9 yr. Ribas et al. (2005) suggested that the high energy luminosity of a young star drops as power-law, whose power indices vary from band to band. Here for simplicity, we assume that the power index is the same $L \propto \min\{1, (t/10^8 \text{ yr})^{-1.5}\}$ in all bands, before totally shutting down radiation at 10^9 yr. For those planet envelopes in the Parker wind zone in Figure 8, we assume that it drops vertically down to the photoevaporative region immediately before evolving them photoevaporatively if $M_c > 3 M_\oplus$, or that it loses all envelope otherwise.

One possible caveat is the evolution of specific entropy in the adiabatic interior of planet atmosphere, characterized by the Kelvin-Helmholtz timescale, τ_{KH} . OW17 suggested that $\tau_{\text{KH}} = \max\{10^8 \text{ yr}, t\}$ at time t during the evolution process. Intuitive as it seems, we realize that this recipe overestimates the overall energy loss of planet envelopes after 10^8 yr, by comparing the evolution of planet radii under OW17 scheme to the detailed simulations, e.g. Howe & Burrows (2015). Hence we simply assume $\tau \simeq 10^8$ yr for all planets at all times. This may overestimate observed planet radii at the same M_{ad} after evaporation, but the post-evaporation M_{ad} may be

underestimated by having a bigger R_{EUV} during the evolution, partially offsetting the former overestimation.

By evolving the ensemble with 10^4 model planets, we obtain the frequency of evolved planet models on the $\{\log_{10} P \times \log_{10} R_p\}$ plane (here R_p is characterized by r_{rcb}), presented in Figure 10. The distribution is bimodal: one peak locates at $R_p \sim 1.4 R_\oplus$, $P \sim 10$ days, and another at $R_p \sim 2.5 R_\oplus$, $P \sim 30$ days. Locations of these two peaks agree semi-quantitatively with observation results in e.g. Fulton et al. (2017); Dong et al. (2017). Similar to OW17, this bimodality is attributed to the peak in evolution timescales at $M_{\text{ad}}/M_c \sim 10^{-2}$, which is hereby confirmed in detailed simulations with hydrodynamics, radiative transfer and thermochemistry involved. The observations also confirm the lack of objects at the upper left corner in the plot, which is a direct result of photoevaporation (e.g. Lundkvist et al. 2016).

8. SUMMARY

In conclusion, this work studies the photoevaporation processes of planet atmosphere by combining 2.5-dimensional axisymmetric full hydrodynamic simulations with consistent thermochemistry and ray-tracing radiative transfer.

As the initial conditions of photoevaporation, static planet envelopes require the atmospheric pressure at large radii being balanced by the ambient; otherwise, the envelopes may lose mass rapidly through Parker wind. We find that for planet core mass $M_c \lesssim 3 M_\oplus$, such balancing is almost impossible to achieve by ambient pressure, which suggests that they may not hold substantial H/He envelopes. Semi-analytic models with spherical symmetry and hydrogen ionization/recombination only suffer from the lack of microphysics and proper hydrodynamics.

Numerical simulations reveal that the wind escape at 32 km s^{-1} with the “standard” high energy radiation prescribed by Ribas et al. (2005) and OW17, for a planet with a $5 M_\oplus$ rocky core and envelope mass fraction 10^{-2} . Such a model planet loses its envelope mass at $\dot{M} \simeq 4 \times 10^{-10} M_\oplus \text{ yr}^{-1}$. While the outflow is fairly close to radial on the day hemisphere, there exists a static tail on the other side, shaped hydrodynamically by the flows near $\theta = \pi/2$. We emphasize the importance of multi-dimensionality by models whose supersonic outflows still survive under strong stellar windram pressure, with comparable mass loss rate to the fiducial case. By turning off radiation flux in different bands, we find that the main determinant of mass loss rate is the EUV photons, which interact with most abundant species, H/H₂/He. Other bands of radiation assists the EUV photons by enlarging the effective interception area of EUV and destroying molecular and atomic coolants. Varying the planet and atmosphere properties confirm that the size of EUV photosphere is the most relevant factor. By setting different incident high energy fluxes, we find that the mass loss rate drops sub-linearly and the kinetic energy super-linearly at low irradiation flux, where the mechanism limiting the outflow is molecular ro-vibrational cooling rather than recombination. Our numerical grid of planet models suggests that the decrease of occurrence in rich planetary atmospheres with core mass $M_c \lesssim 6 M_\oplus$ is likely to be attributed to photoevaporation. Hinted by numerical explorations, we propose a semi-empirical an-

alytic formula for the mass loss rate of photoevaporation, being accurate to $\sim 20\%$ in most cases, enabling further viable predictions, e.g. simulating the evolution of planet ensembles. We semi-quantitatively reproduce the bimodal distribution of Kepler planet on the $\{\log_{10} P \times \log_{10} R_p\}$ plane by evolving such an ensemble, owing to the longest t_{evap} for envelope mass fraction around 10^{-2} .

In future works, we hope to explore the problem using models with consistent thermochemistry in three dimensions. After leaving the planet, photoevaporative outflow is subject to modulations by orbital motion. Orbital centrifugal force and the Coriolis force, which are expected to play a role even within the Hill sphere of a planet in the co-rotational frame, break the axisymmetry assumed in the 2.5-dimensional models in this paper. Specifically,

three dimensional models will help us understand the behavior of the tail, which is particularly interesting as similar structures are already found in observations (e.g. Ehrenreich et al. 2015; Lavie et al. 2017). Moreover, three dimensional simulations will enable us to explore the interaction of photoevaporative outflow with planet spin and even magnetic field, leading to insights on more interesting physics therein.

This work was partially supported by Princeton University's Department of Astrophysical Sciences. We thank our colleagues Xuening Bai and Jeremy Goodman, for discussions and for detailed comments on a preliminary draft.

APPENDIX

A. EQUATIONS FOR SEMI-ANALYTIC MODELS

A.1. Hydrodynamic and microphysical equations

Under spherical symmetry, the hydrodynamic equations read, in steady state (thus $\partial_t \equiv 0$),

$$\begin{aligned} \frac{1}{r^2} \partial_r (r^2 \rho u) &= 0 ; & \frac{1}{r^2} \partial_r (r^2 \rho u^2) &= -\partial_r p - \frac{GM_c \rho}{r^2} ; \\ \frac{1}{r^2} \partial_r \left[r^2 u \left(\gamma E + \frac{\rho u^2}{2} - \frac{GM_c \rho}{r} \right) \right] &= S_E , \end{aligned} \quad (\text{A1})$$

where u is the radial velocity, $E = p/(\gamma - 1)$ the internal energy density of gas. Note that the gas pressure satisfies $p = (1 + x_e) k_B T n$, $n \equiv \rho/m_p$ is the number density of hydrogen nuclei, $x_e \equiv n_e/n$ is the ionized fraction. S_E is the energy source term,

$$S_E = F \sigma n (1 - x_e) (h\nu - I_e) - \alpha_B n^2 x_e^2 \langle E_{\text{rr}} \rangle , \quad (\text{A2})$$

in which the radiation flux F obeys the Lambert-Beer's law,

$$\partial_r \ln F = \sigma n (1 - x_e) . \quad (\text{A3})$$

The conservation of elements, combined with mass conservation, yields,

$$u \partial_r x_e = S_I \equiv F \sigma (1 - x_e) - \alpha_B n x_e^2 . \quad (\text{A4})$$

By specifying reference dimensional variables l_0 , ρ_0 , c_{s0} , and F_0 , the following equalities define the dimensionless parameters (note that Θ and ϵ are *not* independent; the Greek letters of dimensionless quantities here are not to be confused with physical quantities in other sections):

$$\begin{aligned} \lambda &\equiv \frac{r}{l_0} , & \varrho &\equiv \frac{\rho}{\rho_0} , & \Theta &\equiv \frac{T}{T_0} , & \mu &\equiv \frac{u}{c_{s0}} , & \Gamma &\equiv \frac{GM_c}{l_0^2 c_{s0}^2} , & \delta &\equiv \frac{\Delta}{c_{s0}^2} = \mu^2 - \epsilon \varrho^{-1} , & \epsilon &\equiv \frac{\gamma(\gamma - 1)E}{c_{s0}^2 \rho_0} , & \varphi &\equiv \frac{F}{F_0} , \\ \xi_0 &\equiv \frac{\langle E_{\text{rr}} \rangle_{T=T_0}}{k_B T_0} = \frac{3}{2} , & \zeta_0 &\equiv \frac{h\nu - I_e}{I_e} , & \tau_0 &\equiv \frac{\sigma \rho_0 l_0}{m_p} , \\ C_1 &\equiv \frac{F_0 \sigma I_e l_0}{c_{s0}^3 m_p} , & C_2 &\equiv \alpha_0 \left(\frac{\rho_0}{m_p} \right)^2 \left(\frac{k_B T_0 l_0}{\rho_0 c_{s0}^3} \right) , & C_3 &\equiv \frac{F_0 \sigma l_0}{c_{s0}} , & C_4 &\equiv \frac{\alpha_0 l_0 \rho_0}{c_{s0} m_p} . \end{aligned} \quad (\text{A5})$$

Then eqs. (A1) through (A4) are recast in their dimensionless form,

$$\begin{aligned} \partial_\lambda \varrho &= (\mu \delta)^{-1} [(\gamma - 1) \Sigma_E - 2\mu^3 \varrho / \lambda + \Gamma \mu \varrho / \lambda^2] ; \\ \partial_\lambda \mu &= -(\varrho \delta)^{-1} [(\gamma - 1) \Sigma_E - 2\mu \epsilon / \lambda + \Gamma \mu \varrho / \lambda^2] ; \\ \partial_\lambda \epsilon &= \delta^{-1} \gamma [(\gamma - 1) \mu \Sigma_E - 2\mu^2 \epsilon / \lambda + \Gamma \epsilon / \lambda^2] ; \\ \partial_\lambda x_e &= \mu^{-1} \Sigma_I ; \\ \partial_\lambda \varphi &= -\tau_0 \varrho (1 - x_e) \varphi ; \\ \Sigma_E &\equiv C_1 \varphi \varrho (1 - x_e) \zeta_0 - C_2 \Theta^{\kappa+1} x_e^2 \varrho^2 \xi_0 ; \\ \Sigma_I &\equiv C_3 \varphi (1 - x_e) - C_4 \Theta^\kappa x_e^2 \varrho . \end{aligned} \quad (\text{A6})$$

A.2. Critical and boundary conditions

The ordinary differential equations (ODEs) in eqs. (A6) are singular at $\delta = 0$, i.e. the radial velocity becomes transonic. Physically feasible solutions (eigen solutions) must pass through the sonic surface regularly by also having vanishing numerators for $\partial_\lambda \rho$, $\partial_\lambda \mu$ and $\partial_\lambda \epsilon$. It is straightforward to prove that numerators of those derivatives vanish simultaneously if one of them approaches zero as $\delta \rightarrow 0$. Near the sonic surface the approximated derivatives are obtained by the l'Hospital rule. Also, $\mu \rightarrow 0$ leads to singularity where Σ_E is still finite. We construct the solution by starting at a finite radius $\lambda_{\text{ini}} = (r_{\text{ini}}/l_0)$, then integrate both inwards to $\lambda_{\text{min}} = (r_{\text{min}}/l_0)$, defined as the wind base, where the dimensionless radiation flux $\varphi = 10^{-4}$, and outwards to $\lambda_{\text{max}} = (r_{\text{max}}/l_0) = 10\lambda_{\text{ini}}$. The dependent variables at r_{ini} are adjusted, so that the solution (a) is regular at the sonic surface; (b) satisfies $\varphi = 1$ at r_{max} by setting F_0 the incident EUV flux; and (c) matches ρ and T of the given isothermal hydrostatic profile at r_{min} (see also eq. 5).

We are not matching x_e at the inner boundary λ_{min} , as we do not prescribe the ionization profile in the static region, while x_e drops rapidly to zero near and below λ_{min} . Comparing the number of effective constraints (ρ and T at r_{min} , $\varphi = 1$ at r_{max} , and regularity at the sonic point; 4 constraints in total) to the number of dependent variables (ρ , μ , ϵ , x_e , and φ ; 5 dependent variables in total), the ODEs are actually *underdetermined* with one degree of freedom: with identical internal isothermal profile and external radiation, a series of solutions (that are regular at transonic points) can match the isothermal profile at different r_{min} . This mathematical consideration actually has its physical implication, as is elaborated in §3.2.

REFERENCES

- Ádámkóvics, M., Glassgold, A. E., & Najita, J. R. 2014, ApJ, 786, 135
- Bai, X.-N., & Goodman, J. 2009, ApJ, 701, 373
- Borucki, W. J., Koch, D. G., Basri, G., et al. 2011, ApJ, 736, 19
- Bourrier, V., Lecavelier des Etangs, A., Ehrenreich, D., Tanaka, Y. A., & Vidotto, A. A. 2016, A&A, 591, A121
- Carroll-Nellenback, J., Frank, A., Liu, B., et al. 2017, MNRAS, 466, 2458
- Carter, J. A., Agol, E., Chaplin, W. J., et al. 2012, Science, 337, 556
- Christie, D., Arras, P., & Li, Z.-Y. 2016, ApJ, 820, 3
- Dong, S., Xie, J.-W., Zhou, J.-L., Zheng, Z., & Luo, A. 2017, ArXiv e-prints, arXiv:1706.07807
- Draine, B. T. 2011, Physics of the Interstellar and Intergalactic Medium (Princeton University Press)
- Draine, B. T., & Bertoldi, F. 1996, ApJ, 468, 269
- Draine, B. T., & Sutin, B. 1987, ApJ, 320, 803
- Dressing, C. D., Charbonneau, D., Dumusque, X., et al. 2015, ApJ, 800, 135
- Ehrenreich, D., Bourrier, V., Wheatley, P. J., et al. 2015, Nature, 522, 459
- Freedman, R. S., Marley, M. S., & Lodders, K. 2008, ApJS, 174, 504
- Fressin, F., Torres, G., Charbonneau, D., et al. 2013, ApJ, 766, 81
- Fulton, B. J., Petigura, E. A., Howard, A. W., et al. 2017, AJ, 154, 109
- Ginzburg, S., Schlichting, H. E., & Sari, R. 2016, ApJ, 825, 29
- Glover, S. C. O., Federrath, C., Mac Low, M.-M., & Klessen, R. S. 2010, MNRAS, 404, 2
- Goldsmith, P. F. 2001, ApJ, 557, 736
- Gorti, U., & Hollenbach, D. 2008, ApJ, 683, 287
- Hollenbach, D., & McKee, C. F. 1979, ApJS, 41, 555
- Howe, A. R., & Burrows, A. 2015, ApJ, 808, 150
- Igea, J., & Glassgold, A. E. 1999, ApJ, 518, 848
- Ilgner, M., & Nelson, R. P. 2006, A&A, 445, 205
- Jim, S., & Mordasini, C. 2017, ArXiv e-prints, arXiv:1706.00251
- Kwan, J., & Krolik, J. H. 1981, ApJ, 250, 478
- Lammer, H., Selsis, F., Ribas, I., et al. 2003, ApJ, 598, L121
- Lavie, B., Ehrenreich, D., Bourrier, V., et al. 2017, A&A, 605, L7
- Lecavelier Des Etangs, A. 2007, A&A, 461, 1185
- Lecavelier Des Etangs, A., Ehrenreich, D., Vidal-Madjar, A., et al. 2010, A&A, 514, A72
- Li, A., & Draine, B. T. 2001, ApJ, 554, 778
- Lopez, E. D., & Fortney, J. J. 2013, ApJ, 776, 2
- . 2014, ApJ, 792, 1
- López-Morales, M., Haywood, R. D., Coughlin, J. L., et al. 2016, AJ, 152, 204
- López-Puertas, M., Dinelli, B. M., Adriani, A., et al. 2013, ApJ, 770, 132
- Lundkvist, M. S., Kjeldsen, H., Albrecht, S., et al. 2016, Nature Communications, 7, 11201
- Marcy, G. W., Isaacson, H., Howard, A. W., et al. 2014, ApJS, 210, 20
- McElroy, D., Walsh, C., Markwick, A. J., et al. 2013, A&A, 550, A36
- Mignone, A. 2014, Journal of Computational Physics, 270, 784
- Murray-Clay, R. A., Chiang, E. I., & Murray, N. 2009, ApJ, 693, 23, (M-CCM09)
- Neufeld, D. A., & Kaufman, M. J. 1993, ApJ, 418, 263
- Omukai, K., Hosokawa, T., & Yoshida, N. 2010, ApJ, 722, 1793
- Owen, J. E., & Jackson, A. P. 2012, MNRAS, 425, 2931
- Owen, J. E., & Morton, T. D. 2016, ApJ, 819, L10
- Owen, J. E., & Wu, Y. 2013, ApJ, 775, 105
- . 2016, ApJ, 817, 107
- . 2017, ArXiv e-prints, arXiv:1705.10810, (OW17)
- Parker, E. N. 1958, ApJ, 128, 664
- Rafikov, R. R. 2006, ApJ, 648, 666
- Ribas, I., Guinan, E. F., Güdel, M., & Audard, M. 2005, ApJ, 622, 680
- Rogers, L. A. 2015, ApJ, 801, 41
- Rogers, L. A., & Seager, S. 2010, ApJ, 712, 974
- Sanz-Forcada, J., Micela, G., Ribas, I., et al. 2011, A&A, 532, A6
- Tian, F., Toon, O. B., Pavlov, A. A., & De Sterck, H. 2005, ApJ, 621, 1049
- Tielens, A. G. G. M., & Hollenbach, D. 1985, ApJ, 291, 722
- Tripathi, A., Kratter, K. M., Murray-Clay, R. A., & Krumholz, M. R. 2015, ApJ, 808, 173
- Verner, D. A., Ferland, G. J., Korista, K. T., & Yakovlev, D. G. 1996, ApJ, 465, 487
- Verner, D. A., & Yakovlev, D. G. 1995, A&AS, 109
- Visser, R., van Dishoeck, E. F., & Black, J. H. 2009, A&A, 503, 323
- Wang, L., & Goodman, J. 2017, ApJ, 847, 11, (WG17)
- Weingartner, J. C., & Draine, B. T. 2001, ApJS, 134, 263
- White, C. J., Stone, J. M., & Gammie, C. F. 2016, ApJS, 225, 22
- Yelle, R. V. 2004, Icarus, 170, 167
- Zeng, L., Sasselov, D. D., & Jacobsen, S. B. 2016, ApJ, 819, 127